Aerodynamic and Heat Transfer Correlations for Smooth and Rough Airfoils

by

Sepehr SAMADANI

THESIS PRESENTED TO ÉCOLE DE TECHNOLOGIE SUPÉRIEURE
IN PARTIAL FULFILLMENT FOR A MASTER'S DEGREE
IN MECHANICAL ENGINEERING
M.A.Sc.

MONTREAL, JULY 11, 2022

ÉCOLE DE TECHNOLOGIE SUPÉRIEURE
UNIVERSITÉ DU QUÉBEC

BOARD OF EXAMINERS

THIS THESIS HAS BEEN EVALUATED

BY THE FOLLOWING BOARD OF EXAMINERS

Mr. François Morency, Thesis Supervisor
Department of Mechanical Engineering at École de technologie supérieure

Mr. Romain Lemaire, President of the Board of Examiners
Department of Mechanical Engineering at École de technologie supérieure

Mr. Patrice Seers, Member of the jury
Department of Mechanical Engineering at École de technologie supérieure

THIS THESIS WAS PRENSENTED AND DEFENDED

IN THE PRESENCE OF A BOARD OF EXAMINERS AND PUBLIC

11 JULY 2022

AT ÉCOLE DE TECHNOLOGIE SUPÉRIEURE

ACKNOWLEDGMENT

I would like to first express my gratitude to the supervisor of my thesis, Professor François Morency, for his dedication, professionalism, and guidance throughout the period of my masters. Also, my appreciation for having the opportunity to carry out this research.

To my parents, Naser and Naireh for the continuous encouragement throughout my years of study and through the process of researching and writing this thesis. This accomplishment would not have been possible without them I could not have undertaken this journey without their support and their believe in me.

Finally, I want to thank all members of the board of examiners. I am honored to present the results of my research to you.

In the memory of our friend, Zeynab Montazerinejad, PhD student of our research group.

Corrélation entre l'aérodynamique et le transfert de chaleur pour les ailes lisses et rugueuses

Sepehr SAMADANI

RÉSUMÉ

Le problème du givrage sur les avions est connu comme étant l'un des problèmes les plus critiques pour la communauté aéronautique, car il est directement lié à la sécurité des vols. En raison du coût élevé des essais en vol, de nombreuses expériences et des modèles numériques ont été utilisés pour modéliser les conditions de givrage et l'influence sur les conditions de vol. Ainsi, une estimation précise, une estimation précise du transfert de chaleur est nécessaire pour la conception préliminaire des systèmes d'antigivrage et de dégivrage. Par conséquent, l'objectif de cette thèse est de proposer une corrélation pour les profils lisses avant le givrage (systèmes d'antigivrage) et les profils rugueux après l'accrétion de glace (systèmes de dégivrage) afin de prédire le transfert de chaleur, le nombre de Nusselt et le coefficient aérodynamique. La CFD est utilisée comme une méthode haute-fidélité pour prédire le transfert de chaleur sur les ailes lisses et rugueuses, avant et après les conditions de givrage. Pour avoir une meilleure compréhension de la CFD et du givrage des avions, la revue de la littérature de cette thèse est consacrée à une discussion des études sur le givrage et la nécessité de continuer la recherche sur ce sujet, malgré les nombreuses réalisations. La modélisation numérique du givrage est également abordée dans cette section. Le modèle de turbulence Spalart-Allmaras (SA-SMOOTH) pour les profils lisses et le modèle de turbulence Spalart-Allmaras avec modification de la rugosité (SA-ROUGH) pour les profils rugueux sont choisis pour construire la base de données. Avant de construire la base de données sur l'aérodynamique et le transfert de chaleur, les résultats de la CFD sont validés et vérifiés par rapport aux résultats expérimentaux et numériques antérieurs. De plus, pour assurer la fiabilité des résultats, la qualité des maillages est évaluée avec la méthode GCI. La base de données est construite pour les profils NACA 0009, NACA0012, et NACA0015 avec $Reynolds = 0.625 \times 10^6, 1.25 \times 10^6, 2.5 \times 10^6, et\ 5 \times 10^6$ et $0^\circ \leq AOA \leq 13^\circ$ pour les profils lisses et $0^\circ \leq AOA \leq 9^\circ$ pour les profils rugueux. Le nombre de Nusselt et le coefficient de traînée sont ensuite tracés en fonction du coefficient de portance pour en déduire la corrélation. Trois corrélations de coefficient de traînée pour C_d et C_{dmin} pour les profils lisses et C_{dminR} pour les profils rugueux sont proposées avec les trois corrélations de nombre de Nusselt comprenant Nu_{avg} pour les corrélations générales et Nu_{max} et Nu_{maxR} pour les valeurs initiales des profils lisses et rugueux. Pour vérifier la corrélation de transfert de chaleur proposée, elle est comparée à un travail précédent pour la surface lisse.

Mots clés: transfert de chaleur, antigivrage, dégivrage, turbulence, mécanique des fluides numérique

Aerodynamic and Heat Transfer Correlation for the Smooth and Rough Airfoils

Sepehr SAMADANI

ABSTRACT

The problem of icing in aircrafts is known as one of the most critical issues for the aviation community as this matter is directly connected to the flight safety. Due to the high cost of flight tests, many experiments and numerical models have been used to model the icing condition and the influence of the flight. In particular, an accurate estimation of the heat transfer is needed for preliminary design of the anti-icing and de-icing systems. Therefore, the goal of this thesis is to propose a correlation for smooth airfoils before icing (anti-icing systems) and rough airfoils after the ice accretion (de-icing systems) to predict the heat transfer Nusselt number and aerodynamics coefficient. The CFD is used as a high-fidelity method to predict the heat transfer on the smooth and rough airfoils, before and after icing conditions. To have a better understanding of CFD and aircraft icing, the literature review of this thesis is dedicated to a discussion about the history of icing studies and the necessity of continuous icing research, in spite of the numerous achievements. Also, the numerical modelling for icing is discussed in this section. The Spalart-Allmaras turbulence model (SA-SMOOTH) for the smooth airfoils and the Spalart-Allmaras turbulence model with the roughness modification (SA-ROUGH) for the rough airfoils are chosen to build the database. Before building the aerodynamics and heat transfer database, the CFD results are validated and verified against prior experimental and numerical results. Also, to ensure the reliability of the results, the quality of the meshes are evaluated with the GCI method. The database is built for the NACA 0009, NACA0012, and NACA0015 airfoils with $Reynolds = 0.625 \times 10^6, 1.25 \times 10^6, 2.5 \times 10^6, and\ 5 \times 10^6$ and $0^\circ \leq AOA \leq 13^\circ$ for the smooth and $0^\circ \leq AOA \leq 9^\circ$ for the rough airfoils. The Nusselt number and the drag coefficient are then plotted as a function of the lift coefficient to derive the correlation. Three drag coefficient correlations for the C_d and C_{dmin} for the smooth and C_{dminR} for the rough airfoils are proposed with three Nusselt number correlations including Nu_{avg} for the general correlations and Nu_{max} and Nu_{maxR} for the smooth and rough airfoils initial values. To verify the proposed heat transfer correlation, the new proposed correlation is compared with a previous work for the smooth surface.

Keywords: heat transfer, anti-icing, de-icing, turbulence, Computational Fluid Dynamics

TABLE OF CONTENTS

Page

LIST OF TABLES

Page

LIST OF FIGURES

Page

LIST OF ABREVIATIONS & ACRONYMS

AOA	Angle of Attack
CAST	Commercial Aviation Safety Team
CFD	Computational Fluid Dynamics
DNS	Direct Numerical Simulation
FAA	Federal Aviation Administration
FENSAP-Ice	Finite Element Navier–Stokes Analysis Package for Ice
GCI	Grid Convergence Index
IRT	Icing Research Tunnel
LES	Large Eddy Simulation
LWC	Liquid Water Content
NACA	National Advisory Committee for Aeronautics
NASA	National Aeronautics and Space Administration
NTSB	National Transportation Safety Board
OAT	Outside Air Temperature
RANS	Reynolds Averaged Navier-Stokes Equation
SLD	Supercooled Large Droplets
UAV	Unmanned Aerial Vehicle

LIST OF SYMBOLS AND UNITS OF MEASUREMENTS

$Symbols$:

c_p	$Specific\ heat\ of\ air\ at\ constant\ pressure (KJ.kg^{-1}.K^{-1})$
c_v	$Specific\ heat\ of\ air\ at\ constant\ volume (KJ.kg^{-1}.K^{-1})$
C_l	$Lift\ coefficient$
C_d	$Drag\ coefficient$
c	$Chord\ length\ (m)$
D	$Drag\ force\ (N)$
d	$Distance\ from\ the\ wall\ (m)$
E	$Total\ energy\ per\ unit\ mass\ (J.kg^{-1})$
h	$Enthalpy (J)$
h_s	$Equivalent\ sand\ grain\ roughness\ height\ (m)$
$\widetilde{K}$	$Favre\ averaged\ turbulent\ kinetic\ energy\ (J.kg^{-1})$
$\widetilde{K_{ij}}$	$Favre-averaged\ strain\ rate\ (s^{-1})$
k_{eff}	$Effective\ thermal\ conductivity\ (W.m^{-1}.k^{-1})$
L	$Lift\ force\ (N)$
Ma	$Mach\ number$
Nu	$Nusselt\ number$
P	$Static\ pressure\ (Pa)$
Pr	$Prandtl\ number$
q_w	$Wall\ heat\ flux\ (W.m^{-2})$
R	$Gas\ constant\ for\ air\ (287.06\ j.kg^{-1}.K^{-1})$
Re_s	$Roughness\ Reynolds\ number$
Re_c	$Reynolds\ number\ based\ on\ the\ airfoil\ chord$
T	$Temperature (K)$
V_∞	$Farfield\ velocity\ (m.s^{-1})$

$Greek\ letters$:

ν	$Velocity\ (m/s)$
ρ	$Air\ density\ (kg.m^{-3})$
τ_{ij}	$Viscous\ stress\ (N.m^{-2})$
τ_w	$Wall\ shear\ stress\ (N.m^{-2})$
μ_{tur}	$Turbulent\ dynamic\ viscosity\ or\ eddy\ viscosity\ (N.s.m^{-2})$
γ	$Ratio\ of\ specific\ heat$
μ	$Dynamic\ viscosity\ or\ laminar\ viscosity\ (N.s.m^{-2})$
$\hat{\nu}$	$Eddy-viscosity\ variable$
ν	$Kinematic\ viscosity\ (m^2.s)$
α	$Angle\ of\ attack$
σ	$Adaptative\ dissipation\ function$
$\tilde{\nu}$	$Eddy-viscosity\ variable$

INTRODUCTION

The introduction chapter of this thesis firstly deliberates about the necessity of the in-flight icing studies and the role of ice accretion in the airplane design and safety. A brief history about the ice accretion modelling and the CFD contributions in this regard follows. Finally, the thesis objectives and the method to reach the objectives is presented.

As today, we know that in-flight ice accretions are a result of the low-temperature droplets collection on the surface of an aircraft at the low-altitude clouds. This phenomenon leads to the performance decay and the increase of the fuel consumption at the early stages of the ice accumulation. In the cases when aircraft de-icing systems can not completely eliminate the ice, the ice adhesion may result in the malfunctioning of the control surfaces which is considered as a threat to the flight safety. Therefore, because of the necessity of maintaining the safety at the highest level possible, researchers have investigated to model the process of ice accretions more accurately to improve the aircraft de-icing systems. One of the key points of modelling the ice adhesion on the aircraft is the heat transfer prediction. Research works has focused on improving the heat transfer coefficient predictions during the past decades.

Airplane design and the CFD

From the time that an airplane first materializes as a new thought in the mind of one or more persons to the time that the finished product rolls out of the manufacturer's door, the complete design process has gone through three distinct phases that are carried out in sequence. These phases are, in chronological order, conceptual design, preliminary design, and detailed design (Anderson, 1999).

The conceptual design is the phase when the primary concepts of an aircraft (Ex. aspects of the shape of an aircraft) is determined, and the details are flexible. In the preliminary design, the control systems and the structure of the aircraft will be designed and the Computational Fluid Dynamics (CFD) calculations and the wind tunnel test will be held. The third part of the

design is mainly the “nuts and bolts” design. In this part, aerodynamic, propulsion, structures, performance, and flight control analyses will be finished. In other words, the final precise design is detailed. During the last decades, the operation of aircrafts in all weather conditions, impelled the engineers to improve the flight safety.

Since around the year 1990, CFD has become a commonly used tool in the aircraft industry. Consequently, the CFD calculation as a numerical solution for the aircraft icing has improved and many models have been introduced and validated. These studies have clearly resulted in flying in almost every weather condition and have increased the airplane’s safety. But with accidents like the ATR-72 crash that happened in 1994, the necessity of developing improved ice modelling has been identified (NTSB, 1994). Heat transfer plays a key role in aircraft ice accretion. Consequently, various heat transfer models have been introduced and the numerical methods have improved to solve the heat transfer equations on the wing of an aircraft as a 3-D modelling or an airfoil as a 2-D modelling.

Ice accretion modelling

As the function of aircraft is expanding, aircraft has also been widely applied in various domains such as aerobatic flight, exploration, rescue, private flight, etc., in addition to the primary commercial and military functions. So, it is required that aircraft fly normally in all kinds of weather conditions to accomplish the anticipated assignment (Cao, Wu, Su, & Xu, 2015). For decades, engineers struggled to improve the safety of airplanes. In-flight icing is a threat to both safety and performance of an aircraft.

The icing problems and the threats of this phenomenon has been noticed by various organizations such as the National Aeronautics and Space Administration (NASA), National Transportation Safety Board (NTSB), the Commercial Aviation Safety Team (CAST), the Federal Aviation Administration (FAA), and the National Transportation Safety Board (NTSB). They have made numerous safety operation recommendations. As an example, the NTSB report for the ATR72 accident lists the safety sensitivity revision for the icing systems

and pilot alertness (NTSB, 1994). Moreover, after icing related incidents and accidents, aircraft icing has ranked icing among its "MOST WANTED" Aviation Transportation Safety Improvements (Ratvasky, Barnhart, & Lee, 2010). In-flight icing happens when an aircraft passes through the clouds at the subfreezing temperature that contains cold water droplets. The water droplets impinge on the wing surface and fuselage to create glaze and rime ice (Zhang, Habashi, & Khurram, 2016). Hence, the recommendations and resources, namely the experimental data such as wind tunnel experimental results that were shared by these organizations, have paved the way for the researchers to validate the numerical results with these experimental resources. NASA's Glenn research tunnel is an example of Icing Research Tunnel (IRT), a closed refrigerated loop wind tunnel simulates the icing condition using the spray nozzles.

The aircraft ice protection systems have improved significantly. Nevertheless, according to (Green, 2006) that profiled more than 1000 aviation icing accidents and incidents in the United States between 1978 and 2002, loss of control, stall and hard landings are the severe consequences due to the ice accumulation that leads to the icing incidents and accidents.

There are two types of ice protection for an airplane, de-icing and anti-icing. De-icing is the process of removing frozen contaminants, snow, ice, and/or slush from a surface. Anti-icing is the process of preventing ice formation on the surface of airplanes (Thomas, Cassoni, & MacArthur, 1996). One form of ground anti-icing is spraying chemicals on the surface of an aircraft to continuously delay the reformation, or adhesion, of ice for a certain period. De-icing is also defined as the process of ice generation and elimination. Basically, this process allows a thin layer of ice to form on the surface before the removal, the process of ice formation and elimination is then repeated in flight (FAA, 2019).

For addressing the ice accretion issue, at the present, there are three approaches to assess the effect of icing accumulation on the aircraft surface. Based on (Cao et al., 2015), flight test, wind tunnel experiment, and numerical simulation approaches are considered to obtain the aerodynamic data for in-flight icing, as indicated in Figure 0.1. For the flight test, some

attitudes of the flight are adjusted to acquire the flight data. Based on the origin of the ice, two flight test categories exist: “natural icing condition” and “artificially simulated ice shapes”. The flight test approach is more reliable than the other two approaches but at a relatively higher cost. Putting the test elements (aircraft, wing, or airfoil) in the wind tunnel is the next approach. Since it is expensive and hard to set up an icing tunnel, the usual approach is to predict the ice shape with the icing tunnel and assess the simulated ice shape aerodynamic coefficients in the wind tunnels. Because of the limits and the cost of the first two approaches, the CFD has become more popular in the last decades and it has been increasingly applied in the fluid analysis (Zhang & Romzek, 2008).

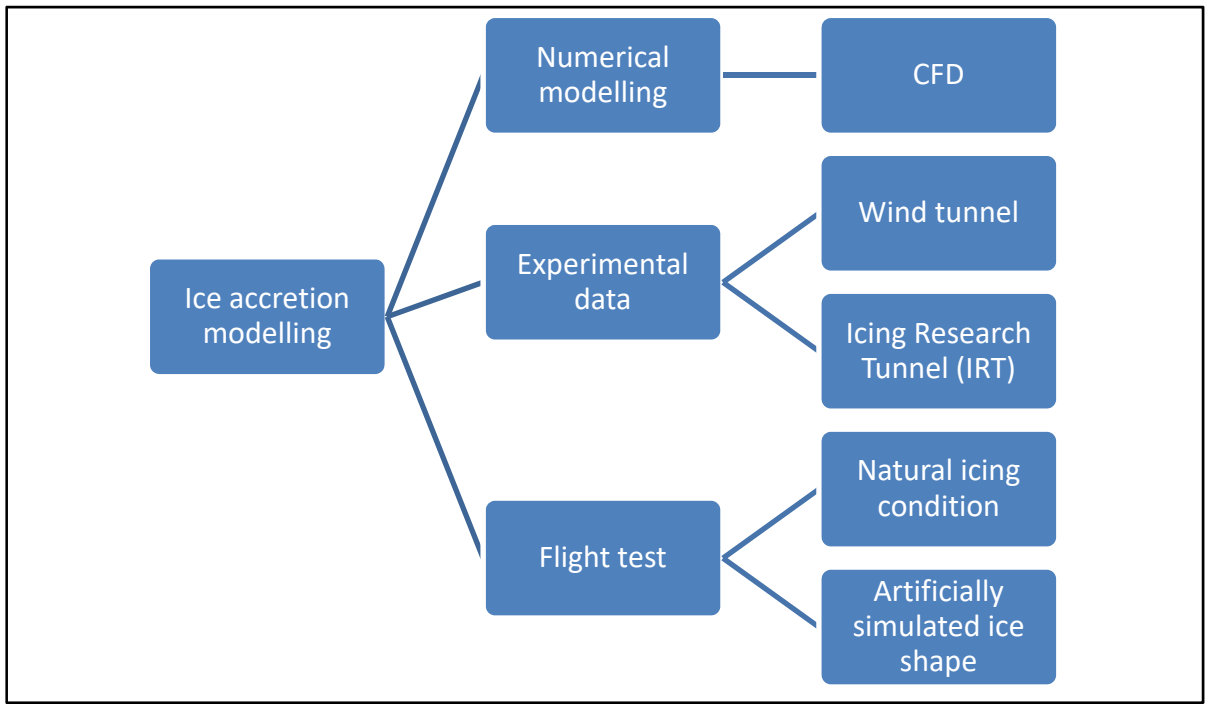

Figure 0.1 Ice accretion modelling

Thesis objectives

To address the challenges of the ice accretion problem, an investigation of the heat transfer and aerodynamics coefficients for the smooth and rough airfoil surface is planned and executed. The main objective of this dissertation research is to study the effects of the surface roughness, namely on the lift and drag correlation and the Nusselt correlation on three airfoils, the NACA 0009, NACA 0012 and NACA 0015. The true benefit of this research might be the new correlation proposed for the Nusselt number based on the lift coefficient for the rough and smooth airfoil. The prediction of the heat transfer is a key element for the appropriate design of anti-icing or de-icing devices.

According to the study of (Bragg, Broeren, & Blumenthal, 2005), roughness is formed at the early stages of the ice accretion. The roughness formation due to the ice accretion then leads to the lift coefficient decrease and changes the heat transfer coefficients at the surface. As we could see in the work of Gulick (Gulick, 1938) a reduction of 25% in the maximum lift is observed in the experiments that he performed. Therefore, the knowledge of the change of the heat coefficient and aerodynamic characteristics due to the rough airfoil would help us to model the ice accretion. It is hoped that the suggested correlation for the heat transfer and aerodynamics coefficients could be applied to model the heat transfer over smooth and rough airfoils. The prediction of the heat transfer is a key element for the appropriate design of anti-icing or de-icing devices

In order to achieve the main objective, the following sub-objectives and methods are carried out:

- Select a mesh density and verify the meshes including errors using the GCI method.
- Build a database for heat transfer over smooth and rough airfoils (NACA0009, NACA0012, and NACA 0015) in a variety of angles of attack and Reynolds numbers using 2D CFD simulations and validate the results.
- Suggest a correlation for the average Nusselt number and the drag coefficient as a function of the lift coefficient using a curve fitting method.

Thesis plan

This thesis is mainly focused on developing a correlation between the aerodynamic coefficients and the heat transfer coefficient for both smooth and rough surfaces of the airfoil. The flow around the airfoils is modelled with CFD and the Reynolds Averaged Navier-Stokes Equation (RANS). For modelling the roughness on the wall, due to the numerous rough models and heat transfer models, this thesis should be considered as a contribution to the "best practice" of rough and smooth airfoil comparison. The entire thesis is composed of three chapters and is organized as follows:

In **chapter 1**, the different ice shapes, the impact of each type of ice on the flight, and a brief history of aircraft icing are discussed. Afterwards, the numerical modelling in aircraft icing with the computer's development is discussed following the evolution of the RANS equations from the original model to the Spalart-Allmaras turbulence model and the rough Spalart-Allmaras turbulence model. The thermal models to account for the roughness effects are then argued. Subsequently, the last section of the literature review chapter discusses the previous works about the derivation of the correlations for the aerodynamic coefficients and heat transfer coefficients.

Chapter 2 outlines the implemented models to solve the problem. At first, the widely used RANS equations are introduced. Then, the turbulence model is selected as the Spalart-Allmaras with the extension of this model to account for the roughness effects. Later, the 2PP heat transfer model is discussed which is a thermal model that accounts for the roughness. In the second part of the chapter, the Grid Convergence Index (GCI) method used for the mesh sensibility study is presented and the boundary conditions of the problem are mentioned.

The validation and verification of the results and the derivation of the correlation for the Nusselt number and the drag coefficient as a function of the lift coefficient are done in **chapter 3**. First the mesh configuration for the three mesh densities is described and the appropriate

meshes are selected with the GCI method. Then, the results for the aerodynamic and heat transfer coefficients are verified against the previous works and validated with experiments. Afterwards, the correlation for the drag coefficient the average Nusselt number based on the lift coefficient and are estimated with the quadratic regressions curve fitting method (MATLAB, 2019). The analysis and the comparison of the heat transfer correlation with the numerical work of (Samad, 2021) follows.

CHAPTER 1

LITERATURE REVIEW

The introduction chapter of this thesis briefly deliberated the role of CFD in the aircraft design and the ice accretion modelling. The main problematic of this research is to propose an aerodynamics and heat transfer correlation since an estimation of the airfoil's heat transfer characteristics is crucial for the design of the ice prevention systems in aircrafts. In this regard, the review of the past works on numerical icing simulation, aerodynamics, and heat transfer correlations from the beginning until the state-of-the-art research are discussed in this chapter.

To have a better understanding of in-flight icing, the necessity of the aircraft icing research is first discussed from several viewpoints, as the safety and aerodynamic performance degradation created by ice accretion. Afterwards, the history of the numerical simulation of aircraft icing is reviewed and the icing models for the ice accretion are discussed. Finally, the heat transfer study on the wings and airfoils are performed and the prior works about the derivation of the heat transfer and aerodynamics correlations are reviewed.

Aircraft icing occurs on the surfaces of some components of an aircraft encountering an icing meteorological condition. Over 50% of commercial airplane accidents are weather-related (Klehr, 1984). Due to the progress in flight simulations and pilot training in severe conditions such as the icing conditions, accidents have decreased compared to the past. Still, major ice accumulation may cause flight accidents (Cao et al., 2015). As an example, CAE Inc, a Canadian manufacturer and developer of aircraft simulator software, is using supercomputers to model the various mereological conditions (Link, Kruk, McKay, Jennings, & Craig, 2002).

A study which analyzed iced aircraft accidents between 1990 and 2000 shows that 12 % (388 cases) of the adverse weather conditions accidents happened under icing conditions. (Buck, 2008) categorizes the clouds into the wet and dry categories. The dry clouds have relatively little moisture and low potential for aircraft icing. However, wet clouds contain the freezing

droplets resulting in ice accretion on aircrafts. Moreover, Montreal and New York are categorized into the high-risk regions for flight icing conditions because of the presence of clouds having a high water droplet density.

Deformation of control surfaces of an aircraft would degrade the aerodynamic effectiveness, resulting in the reduction of the lift and increase of the drag. It is forbidden to fly an aircraft that has frost, ice, or snow attached to its critical surfaces in Canada (Transport-Canada, 2019). The ice accretion is a result of the impinging liquid drops on the aircraft surface. It can occur even when the Outside Air Temperature (OAT) is above 0°C (Transport-Canada, 2019). For in-flight icing, studies show that ice shape depends mostly on the local convective coefficient that is a function of surface roughness (Liu & Hu, 2018).

(Bragg et al., 2005) categorized four different in-flight icing categories based on the ice geometry. An ice shape may be divided into more than one category at the same time in this grouping method. The first ice shape category is ice roughness. i) Ice roughness geometry is smaller than the other types of ice because it happens at the early stages of ice accretion. Therefore, the effect of this type of ice on the aerodynamic characteristics is smaller than the other types. Figure 1.1 shows the ice roughness accumulated on a wing from the study that was conducted in Glenn's IRT on the swept-wing ice accretion characterization (Broeren et al., 2013). The characterization of the ice roughness was studied by (Anderson, 1999). Based on the study of Anderson, the glaze ice and rime ice conditions on the leading edge of an airfoil are divided into three areas: the smooth zone, the rough zone, and the feather region. According to his work, the characteristic of the roughness elements in each zone depends on the accumulation parameters and the associated freezing fractions. ii) The horn ice shape could be identified by its angle with the chord line and the height. The characteristic of this ice shape is the separation bubble that appears downstream of the horn ice that causes a detachment of the flow and then reattaches further downstream on the airfoil based on the size of the horn ice. iii) Streamwise ice shape has the minimum aerodynamic effect after roughness ice accretion. The ice accretion follows the contour of the airfoil. iv) The spanwise-ridge ice has a more pronounced 3D shape when compared to the horn shape, the streamwise, and the 2D ice

roughness geometry. This type of ice usually occurs when the ice protection system fails to totally evaporate the supercooled large droplets (SLD)'s that impinge on the leading edge of the wing and runback icing happens. This ice shape usually formed due to the malfunctioning of the de-icing system. The droplets run back from the leading edge and freeze downstream on the wing of the airplane and cause this type of ice formation. This type of ice accretion is a bigger threat to flight safety due to the disastrous aerodynamic effect (Cao et al., 2015).

Figure 1.1 The initial roughness formed on NACA 0012 at NASA's Glenn IRT
Taken from Broeren et al. (2013, p. 6)

As mentioned, anti-icing systems prevent the formation of ice before facing icing conditions and de-icing systems remove the ice shapes after accretion on aircrafts. The heating pads and the inflating systems are the de-icing systems that are used in aircraft. The heating pad de-icing is the process of ice removal with the electrical resistance heating elements. While the inflating

de-icing systems remove the ice by inflating rubber membranes that are filled with the pressurized air over the surface of the wing. When activated, inflating devices increase the drag force due to the shape change of the wing.

Ice accretion studies began in 1920 (Bragg et al., 2005). At the beginning of the in-flight ice studies, it was found that this phenomenon has more drawbacks than just the excess weight to the aircraft. The formation of ice upon airplanes in flight on the propeller VE-7 aircraft was studied by (Carroll & McAvoy, 1929). They found out that the reduction of the aerodynamic efficiency due to the ice accretion on the aircraft is more critical than the additional weight. In 1938, a NACA 0012 airfoil was tested in the Langley Memorial Aeronautical Laboratory that showed the maximum lift coefficient reduced from 1.32 to 0.80 (25%) and the drag coefficient increased by 90% for the tested condition (Gulick, 1938). Later in 1944, the first icing research tunnel was built at the Lewis Flight Propulsion Laboratory by NACA, and the tunnel with the spray nozzles was conducted in 1950 (Bragg et al., 2005). A series of experiments were conducted by (Gray, 1958) with the NACA 65A004 airfoil in the IRT starting in 1953. In these experiments, ice accumulates in a controlled condition enabling the development of a correlation to evaluate the change in drag due to icing formation.

1.1 Numerical simulation of aircraft icing

The numerical simulation goal is to model the pattern of the ice accumulation to be able to retrieve the aerodynamic characteristics of the airfoil or wing. The aerodynamic effects of in-flight icing are the reduction of the stall angle and the increase of the drag. With the development of the CFD, the numerical simulation of ice accretion began in the 1980s (Cao et al., 2015). They generalized the procedure of the numerical simulation approach for ice shape prediction into three steps: 1) calculation of the pressure, temperature, and velocity around the wing or the airfoil in the flowfield; 2) resolution of the governing equations to compute the droplet impingement characteristics in order to determine the motion of supercooled droplets in the flowfield; and 3) resolution of the ice accretion models according to mass and energy conservation laws, to simulate the ice accretion, and to obtain the ice shapes.

According to (Bragg et al., 2005) the first key moment in the aircraft icing numerical simulation history is 1979. At this time, the numerical icing study began under the influence of the NASA aircraft-icing program. The second key point is the ATR-72 accident in 1994 that changed the focus of aerodynamic study from scientific exercise to aircraft safety.

With the development of computers and the ability for solving aeronautical problems, the CFD became widely used (Cao et al., 2015). Particularly, by solving numerically the Navier-Stokes equations, using the time-average method called the Reynolds Average Navier Stokes model which is used with turbulence models to solve the Reynolds stress (Blazek, 2015). Due to the limitations and the expenses of the flight tests and wind/ice tunnel tests, the numerical simulations became more important in comparison to the other certification conditions (Beaugendre, Morency, Habashi, & Benquet, 2003). Hence, researchers were attracted to deploy numerical simulations for solving the Navier-Stokes equations in the case of aircraft icing.

Besides the RANS model, Direct Numerical Simulation (DNS) and Large Eddy Simulation (LES) are two turbulence modeling approaches that can produce detailed structures of turbulence. DNS is the most detailed approach that uses the numerical discretization to solve the Navier-Stokes equations without any approximation and simplification. Because of the cost of numerical calculations, DNS is only applicable for low Reynolds number flows. In LES approach the large-scale turbulence motions are directly solved while the small motions are modelled. Although the DNS and LES simulations are more detailed and accurate that RANS, they are relatively computationally expensive and most of the industrial needs are satisfied with the RANS turbulence modelling (Blazek, 2015).

Through the evolution of the CFD, we could see numerical simulations have evolved from application at the high-speed cruise conditions to the full flight envelope. Moreover, CFD could be applied to model the structures, propulsion system components, flight controls, and aerodynamics together, which have closer connections (Tinoco et al., 2005).

While the first generation of the in-flight icing calculation had limitations for the three-dimensional geometries, this problem was solved after due to the development of computers and evolution of the CFD 3D modelling (Bragg et al., 2005). Commonly used ice accretion codes model the water droplet impingement on the surface of the airfoil using either the Eulerian or Lagrangian droplet equation formulations. The Finite Element Navier–Stokes Analysis Package for Ice (FENSAP-ICE) is an in-flight three-dimensional icing model based on the RANS equations in order to solve the flow, the impingement, the ice accretion, the heat loads, and the performance degradation (Beaugendre et al., 2003). Another icing code, LEWICE, uses the physical condition of the flow and the geometry and meteorological parameters of Liquid Water Content (LWC) to predict the shape of the ice accretion.

1.2 Roughness effects with RANS model

A rich literature review that includes the history of the roughness study is done by (Morency & Beaugendre, 2020). As discussed, the in-flight ice accretion models are using convective coefficients to predict the ice accretion. In 2018 (Liu & Hu, 2018) conducted an experiment with the NACA0012 airfoil at Iowa State University IRT in the controlled temperature and velocity under unsteady conditions. Using the Infrared (IR) thermal imaging system, they captured the temperature over the ice accreting airfoil. They found out that the ice shape depends on the convective heat transfer coefficient.

The heat transfer coefficient depends on several factors in addition to the temperature difference between the wing surface and the outside air. First, the boundary layer can be laminar, transitional, turbulent, or separated. It strongly depends on the Reynolds number, angle of attack, and the surface roughness. The heat transfer rates are related to the local skin friction coefficient, and the surface geometry (Lynch & Khodadoust, 2001).

(Dipprey & Sabersky, 1963) conducted a series of experiments in a rough tube to introduce a heat transfer model over the rough surfaces at various temperatures and Reynolds numbers.

Based on their results, they presented the Stanton number, depending on the Prandtl number and Reynolds number. (Healzer, Moffat, & Kays, 1974) showed that the Stanton number and the skin friction coefficient are independent of the velocity. (Kays, 2012) used the roughness Reynold's number from the shear velocity and implemented the Stanton number which was also suggested by (Dipprey & Sabersky, 1963) to calculate the shifted temperature at the wall and the heat transfer above the wall.

Three approaches are considered to calculate the heat transfer over the rough surfaces and are named "highest fidelity", "discrete element approach", and "equivalent sand grain" (Aupoix, 2015). The "highest fidelity" approach consists of calculating the flow around the rough elements using a LES and DNS approach but due to the calculation cost, it is only used in research. The discrete element approach modifies the averaged flow equations to account for the roughness. The third approach, the "equivalent sand grain" was firstly introduced by (Nikuradse, 1950). He conducted a series of experiments with two rough and smooth pipes and presented the resistance factor by measuring the dependence of the flow to the roughness. Moreover, he found that the resistance factor is independent of the roughness at low Reynolds numbers.

Although the early studies by (Anderson & Shin, 1997) show that icing roughness depends on two dimensionless parameters that are the freezing fraction and the accumulation parameter, the sand grain roughness is the single parameter used in the common practice of the ice roughness studies (Han & Palacios, 2017). For the CFD icing calculations, the sand grain roughness adds to the distance of the wall and changes the boundary condition. Therefore, the convective heat transfer increase and change the resulting ice shape (Beaugendre et al., 2003).

For the RANS turbulence model, (Aupoix & Spalart, 2003) proposed an extension to the Spalart-Allmaras turbulence model with the non-zero viscosity at the wall which was developed by Boeing. In this model, the flow is averaged over the roughness elements of the surface with the equivalent sand grain roughness instead of discretizing the flow around each

element. This model is sufficient to predict the shear stress at the wall, but additional corrections are needed to model the heat transfer.

1.3 Thermal model

The extension of the Spalart-Allmaras turbulence model that takes into accounts roughness by (Aupoix & Spalart, 2003) could predict the shear stress at the wall but additional model was needed to model the heat transfer at the rough wall (Morency & Beaugendre, 2020). The three and two parameter models have been proposed for the heat transfer at the surface of a rough airfoil.

The first heat transfer model based on increasing the turbulent Prandtl number at the wall was proposed by (Suga, Craft, & Iacovides, 2006) to take roughness into account and validated for a range of Reynolds numbers and roughness element sizes. As in the energy equation, the turbulent Prandtl number decreases on the rough surfaces because the fluid is trapped at the bottom of the roughness elements. The suggested model increases locally the Prandtl number to compensate for this decrease by considering an additional parameter, the roughness height.

The three parameter models based on the equivalent sand grain roughness, the roughness height, and the surface correction coefficient is proposed by (Aupoix, 2015) and validated and calibrated with the experimental and the numerical data. The new model improves the thermal boundary layer based on implementing the local turbulent Prandtl number to the rough wall calculations.

The other heat transfer model based on the work of (Suga et al., 2006) is proposed by (Morency & Beaugendre, 2020). This model was developed based on the temperature shift at the wall and relies on the roughness height and the equivalent sand grain roughness to model the heat transfer at the wall. The temperature shift at the wall is modelled by increasing the Prandtl number in a way that heat transfer is reduced and calibrated.

In the recent study, (Villeneuve, Samad, Volat, Béland, & Lapalme, 2022) conducted an experiment to measure the heat transfer on a Bell APT70 drone rotor in the icing condition. For the measurement tool, they used the Liquid Water Content (LWC) to measure the liquid content in the air. To assess the effect of the ice accumulation on the UAV, the coefficient of torque and thrust are measured as a function of time before and after the ice accretion on the airfoil.

1.4 Aerodynamics and heat transfer correlation

1.4.1 Aerodynamic correlation

The correlations between the lift coefficient and the drag coefficient have come a long way since the beginning of the aeronautic studies. Various literatures mentioned the correlation between these two coefficients. From CFD results, (Gudmundsson, 2013) proposed a correlation between the lift coefficient and the drag coefficient for 3-D wings and 2-D airfoils based on the curve fitting method for the lift-drag coefficient curve. (Hoerner, 1965) also proposed a lift-drag correlation for the smooth airfoils in which the increase of the drag coefficient is a function of the square of the lift coefficient.

For the rough airfoils, (Gray, 1958) measured the effect of ice accretion on the drag coefficient for the NACA 65A004 airfoil. Based on the ice impingement experimental results, his data was gathered for different angles of attack and different ice shapes and allowed derivating the drag correlation based on the ice parameters and the angle of attack . (Bragg, 1981) conducted a parametric study on different ice shapes such as the ice roughness and horn ice. His studies were used later by others to predict ice shapes and aerodynamic effects of ice accretions.

(Battisti, Zanne, Castelli, Bianchini, & Brighenti, 2020) and (Bianchini et al., 2016) studied turbine blades and analyzed the aerodynamics coefficients for various range of angles of attack. (Bianchini et al., 2016) gathered the CFD data for the NACA 0018 airfoil for the wide range of -180 up to the +180 angles of attack. Then, post-stall correlations for the drag coefficient

were used to verify the CFD results. Later, (Battisti et al., 2020) studied on the drag coefficient correlation for the range of $0 \leq AOA \leq 90$ for the symmetric and asymmetric airfoils. They introduced an extension to the past drag correlations based on the airfoil shape effects and derived a drag coefficient correlation as a function of the angle of attack for the airfoils.

Another study on the Unmanned Aerial Vehicle (UAV) is conducted by (Götten, Havermann, Braun, Marino, & Bil, 2020). They introduced drag coefficient correlation as a function of the friction drag coefficient and pressure drag coefficient. The friction drag coefficient is defined as a function of the skin friction coefficient and the shape of the airfoil which is defined with the Form Factor (FF) term. The pressure drag coefficient is a function of the relative thickness, Reynolds number, and camber derived from the results of the numerical study. Finally, results were validated against the experimental measurements.

1.4.2 Heat transfer coefficient

Heat transfer with imposed heat or temperature at the wall as a tool for calculating heat transfer coefficients over bodies such as a flat plate, cylinder, and airfoil has been used by many. With a constant temperature or heat flux, the heat transfer could be calculated.

(Poinsatte, Van Fossen, & De Witt, 1990) conducted a series of experiments over the NACA 0012 airfoil with smooth and rough surfaces at the NASA Lewis Icing Research Tunnel and published the result for the local Nusselt number and local Frossling number. The experimental data are used to study the roughness effects on the NACA0012 airfoil (Poinsatte, Van Fossen, & De Witt, 1991). They found that the increase of the wall roughness has a direct relation with the heat transfer. In other word, the disturbance of the laminar boundary layer triggers the transition to the turbulent boundary layer in some cases. The roughness element was believed to be the reason for the higher heat transfer for the cases of rough NACA0012. Another study of the performance degradation with ice accretions was conducted by (Henry, Guffond, Garnier, & Bouveret, 2000). The heat transfer for the ice accretions was measured over the

smooth and rough iced airfoil that was heated with a laser source. As the result of the study, it was found that the heat transfer coefficient strongly depends on the surface condition.

For the convective heat transfer, correlations have been proposed for flat plates, cylinders, and airfoils. (Bergman, Incropera, DeWitt, & Lavine, 2011) compiled a set of the Nusselt correlation as a function of the Reynolds number and Prandtl number for simple geometries such as a flat plate, cylinder, and sphere for the external flow conditions.

(Hilpert, 1933) was among the first to suggest a correlation for the Nusselt number for a cylinder in a crossflow. Based on his work, the cylinder heat transfer depends on the Prandtl number and Reynolds number. For iced airfoils, (Wang, Naterer, & Bibeau, 2008) derived correlations for the average Nusselt number as a function of the Reynolds number, angle of attack, and the Prandtl number based on the work of Hilbert. The correlation was based on the experimental NACA 63-421 results with the inside heated and the outside cooled. Twenty-five thermocouples measured the temperature along the airfoil on the inner and outer surface.

For the smooth surface (Samad, 2021) developed the BEMT-RHT and UVLM-RHT methods for calculating the heat transfer over the rotor blades of helicopters and validated the results with experiments. Afterwards, using CFD, he calculated the average and maximum Frossling number over the airfoil for a range of Reynolds numbers and angles of attack. Based on the CFD results and previous works, he proposed a correlation between the maximum Frossling number and the angle of attack for $0 \leq AOA \leq 16$ (pre-stall) and $1 \times 10^5 \leq Re \leq 3 \times 10^6$. Also, a second correlation was also proposed between the average Frossling number and angle of attack for the range of $0 \leq AOA \leq 30$ and $1 \times 10^5 \leq Re \leq 3 \times 10^6$.

Based on the reviewed literature, correlations between the aerodynamic coefficients and the heat transfer coefficients were proposed for different airfoils. However, correlations for airfoils that links smooth and rough surfaces are lacking. Although the rough airfoil aerodynamics and heat transfer correlation may seem a small step in this knowledge, it is beneficial for the

understanding of the roughness effect on the airfoil aerodynamic performance and heat transfer.

CHAPTER 2

MATHEMATICAL MODEL AND NUMERICAL METHOD

In chapter 1, a brief history about the in-flight icing and the icing models was discussed, together with in-flight icing numerical models. As mentioned, ice accretions will result in aerodynamic performance degradations at least. In some cases, this phenomenon resulted in an accident for the aircraft, such as the ATR-72 crash that happened in 1994. Therefore, various models either Eulerian (FENSAP-ICE (Beaugendre et al., 2003) – ONERA (Montreuil et al., 2009)) or Lagrangian (LEWICE (Wright, 2008) – ONERA (Guffond & Brunet, 1988)) approaches have been introduced to predict water impingement during in-flight icing more accurately. Once the mass of impinging water known, the ice accretion strongly depends on the convective heat transfer coefficient which is a function of the surface roughness (Liu & Hu, 2018). In this thesis, the equivalent sand grain roughness and the roughness height are used to evaluate the roughness effects on the flowfield.

The main goal of this chapter is to select a mathematical model for building the heat transfer database for the smooth and rough airfoils. Specifically, this chapter has two main objectives. The first is to present a mathematical model for the turbulent flow with the smooth surface and extend the model for the rough airfoil. Then, the second objective is to select a method to study the mesh effect on the solution when the mesh density increases. In this chapter, first the viscous and thermal models and the numerical method for solving the CFD problems of the thesis is discussed. Then using SU2 software (Palacios et al., 2013), the problems are solved and the solutions are used in the next chapter.

For the smooth solution, the Spalart-Allmaras (SA) turbulence model (Spalart & Allmaras, 1992) is used with the RANS equation, while for the rough airfoil solution, an extension to the SA model is activated to take into account the roughness height and the equivalent sand grain roughness to model the heat transfer over the airfoil. The Prandtl correction model, called the

2PP model is then selected as the turbulent heat transfer model (Morency & Beaugendre, 2020).

First, the GCI method is used to select a good-quality mesh to build the database. Second, the calculation analysis studies the lift and drag coefficients, the Nusselt number and the averaged form of the Nusselt number for the heat transfer coefficient. Then, previous works on the lift and drag coefficient correlation and the heat transfer correlation are introduced. The suggested format for the correlations is introduced based on the limitations and recommendations of the previous works. In the last part of this chapter, the boundary conditions, the numerical methods that are used to discretize the mathematical model together with the computational domain is discussed.

2.1 Problem definition

As mentioned in chapter 1, when a plane passes through the low-altitude clouds containing supeprcooled droplets, the ice forms on the surface on the airplane. Therefore, ice accretions may happen on the critical surfaces of an aircraft such as the hydraulic and pneumatic control surfaces, resulting in the malfunctioning of the flight controls. Figure 2.1 shows an airplane facing icing conditions with the indicated lift force (L) and drag force (D). As mentioned, the icing condition problems happen at low-altitudes, when the aircraft took off and is climbing at hight angle of attack (AOA).

Although the actual problem of the aircraft icing considers a wing with a varying chord size over the wingspan, to model the ice accretion and heat transfer, the wing is modelled with a 2D airfoil shape with a constant chord line (c) and infinite span length. The NACA 0009, NACA 0012, and NACA 0015 airfoils with both smooth and rough surfaces are considered for the study in this thesis. Figure 2.2 shows a 2-D airfoil with an infinite span length and a constant roughness distribution over the airfoil with an AOA between the chord and the velocity.

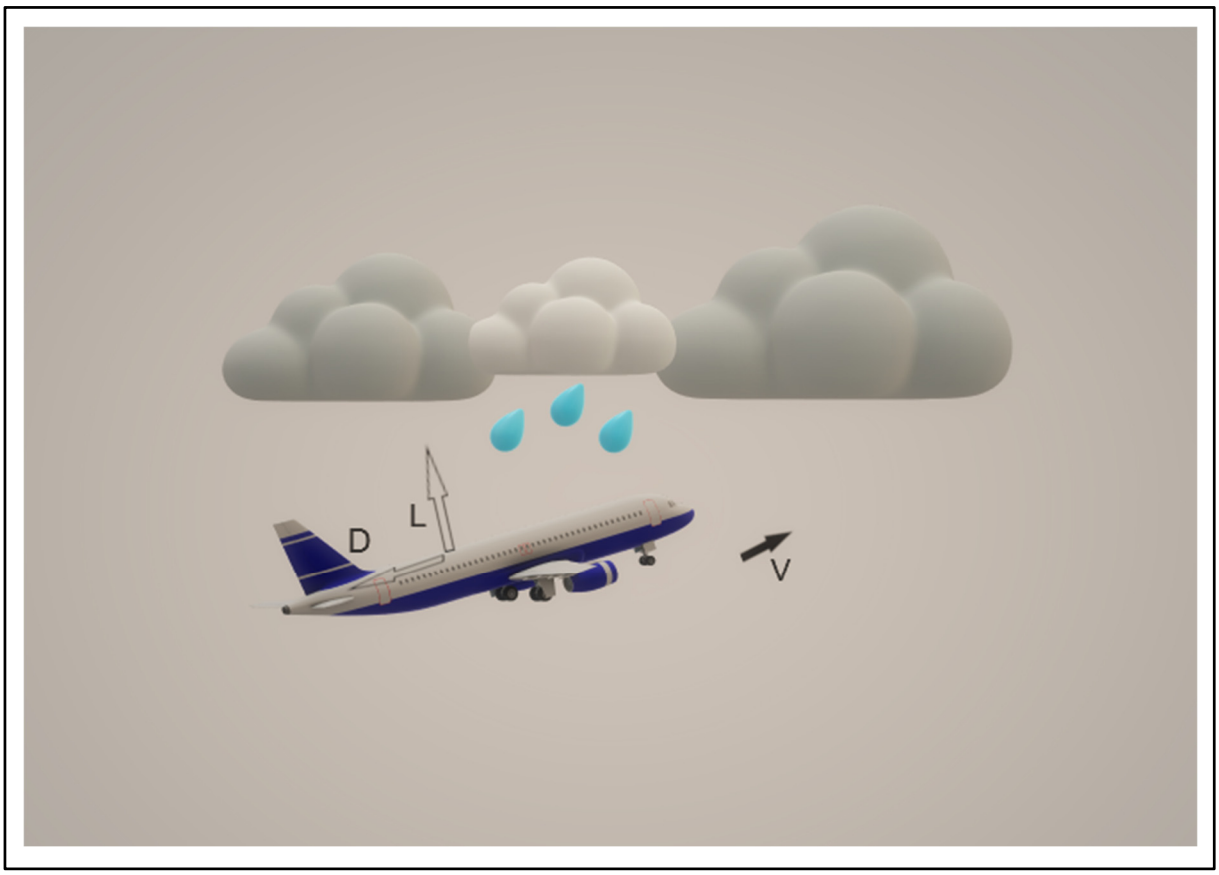

Figure 2.1 Scheme of the actual problem

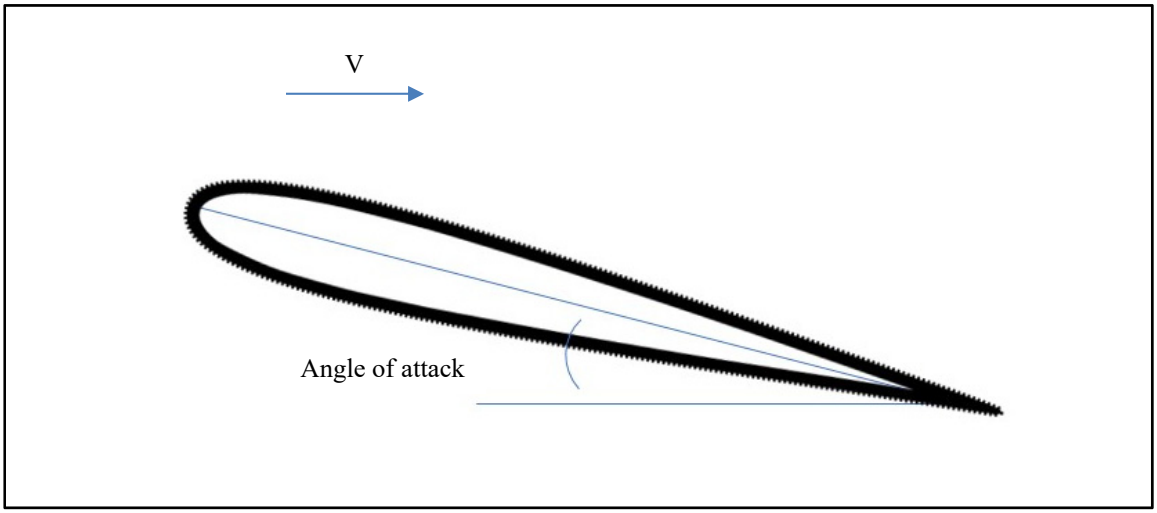

Figure 2.2 Scheme of the rough airfoil and angle of attack (AOA) definition

For the rough airfoil, it is expected that the highest lift coefficient decreases. The AOA at the highest lift coefficient, called the stall angle, also decreases. As shown in Figure 2.2, the problem is modelled with an infinite wing. In order to derive the correlation between the lift coefficient and the heat transfer coefficient, a database will be created for the NACA 0009, NACA 0012, and NACA 0015 airfoils with smooth and rough surfaces. Four Reynolds numbers within the range of $0.625 \times 10^6 < Re < 5 \times 10^6$ are considered for the test cases. Also, the range of the angles of attack varies from $0^{\circ} < AOA < 13^{\circ}$ for the smooth airfoils. For the rough airfoils, the stall angle study will be conducted in the next chapter to determine the AOA range for the database.

As the first step in building the database, the three airfoils are solved with the RANS equations and the Spalart-Allmaras turbulence model. For the rough airfoils the roughness is modelled with the equivalent sand rain roughness and the Spalart-Allmaras turbulence model with the roughness extension. The roughness height is also considered in order to model the heat transfer on the rough airfoil.

2.2 Mathematical model

2.2.1 Reynolds Averaged Navier-Stokes (RANS)

As stated by (Kundu, Cohen, & Dowling, 2015), most of the macroscopic flows in engineering problems are turbulent which leads to the non-linear behavior of fluids. Due to the essence of turbulence, analytical solutions are limited to the fundamental and simple applications such as the flow over a flat plate (Davidson, 2018). As mentioned in chapter 1, due to the high cost of the wind tunnel experiments for a full-body aircraft, researchers have become more interested in the wind tunnel experiments and the numerical simulations. Over the past decades, as an emergence of the highly turbulent problems such as the turbojet and turbofan engines in aircraft and the necessity of optimization with a numerical method, various numerical simulation methods have been proposed to solve turbulent flows. The most common methodology in turbulence modelling is the RANS approach which was proposed based on the knowledge of

the turbulent flow properties. It gives an approximate time-averaged solution to the Navier-Stokes equations.

Reynolds proposed to average the equations of motion by decomposition of the flow variables into the mean and the fluctuating parts. According to Blazek (Blazek, 2015) the Favre decomposition is suggested instead of Reynolds averaging as the density is not constant for the compressible flow except for the pressure and density which results in:

$$\begin{gathered}\frac{\partial \bar{\rho}}{\partial t}+\frac{\partial}{\partial x_i}(\bar{\rho}\tilde{v}_i)=0 \\ \frac{\partial}{\partial t}(\bar{\rho}\tilde{v}_i)+\frac{\partial}{\partial x_j}\left(\bar{\rho}\tilde{v}_j\tilde{v}_i\right)=-\frac{\partial \bar{p}}{\partial x_i}+\frac{\partial}{\partial x_j}\left(\tilde{\tau}_{ij}-\bar{\rho}\widetilde{v_i''v_j''}\right) \\ \frac{\partial}{\partial t}\left(\bar{\rho}\tilde{E}\right)+\frac{\partial}{\partial x_j}\left(\bar{\rho}\tilde{v}_j\tilde{H}\right)=\frac{\partial}{\partial x_j}\left(k\frac{\partial \tilde{T}}{\partial x_j}-\bar{\rho}\widetilde{v_j''h''}+\widetilde{\tau_{ij}v_i''}-\bar{\rho}\widetilde{v_j''K}\right)+ \\ \frac{\partial}{\partial x_j}[\widetilde{v_i}\left(\tilde{\tau}_{ij}-\bar{\rho}\widetilde{v_i''v_j''}\right)]\end{gathered} \tag{2.1}$$

Therefore, Equation (2.1) is the Favre and Reynolds averaged Navier-Stokes where $\tilde{E}$ and $\tilde{H}$ are the total energy and enthalpy respectively and the physical definitions are (Blazek, 2015): $\frac{\partial}{\partial x_i}\left(k\frac{\partial \tilde{T}}{\partial x_j}\right)$ is the molecular diffusion of heat, $\frac{\partial}{\partial x_i}\left(\bar{\rho}\widetilde{v_j''h''}\right)$ is the turbulent transport of heat, $\frac{\partial}{\partial x_i}\left(\bar{\rho}\widetilde{\tau_{ij}v_i''}\right)$ is the molecular diffusion of $\widetilde{K}$, $\frac{\partial}{\partial x_i}\left(\widetilde{v_j''K}\right)$ is the turbulent transport of $\widetilde{K}$, $\frac{\partial}{\partial x_j}\left(\widetilde{v_i}\tilde{\tau}_{ij}\right)$ is the molecular stresses work, $\bar{\rho}$ is the main density, h is the enthalpy $\tilde{v}_i$ is the main velocity, and $\widetilde{K}$ is the Favre averaged turbulent kinetic energy. Also, the bar indicates the Reynolds-averaged values, the double prime stands for the fluctuating parts, and the tilde is used for the Favre-averaged terms. For the compressible flow, the momentum transfer is defined based on the Boussinesq eddy viscosity hypothesis (Blazek, 2015). Therefore, the Favre-averaged Reynolds tensor is defined as follows:

$$\tau_{ij}^{F}=-\bar{\rho}\widetilde{v_i''v_j''}=2\mu_{tur}\tilde{S}_{ij}-\left(\frac{2\mu_T}{3}\right)\frac{\partial v_k}{\partial x_k}\delta_{ij}-\frac{2}{3}\bar{\rho}\widetilde{K}\delta_{ij} \tag{2.2}$$

where μ_{tur}, $\tilde{S}_{ij}$ represent the turbulent eddy viscosity and Favre-averaged strain rate. The total enthalpy is calculated as follows:

$$H = c_p T \tag{2.3}$$

$$R = c_p - c_v \tag{2.4}$$

And the ratio of specific heat:

$$\gamma = \frac{c_p}{c_v} \tag{2.5}$$

2.2.2 The Spalart-Allmaras turbulence model

The term μ_{turb} of the RANS equation is predicted by various turbulence models. The $k - \varepsilon$ and $k - \omega$ turbulence models were the first models that suggested to solve the eddy viscosity by solving two equations. The $k - \varepsilon$ model was presented by (Launder & Spalding, 1983).

Later, the one-equation model by (Spalart & Allmaras, 1992) was developed to compute the eddy viscosity with one equation. The so-called SA model is used in SU2 (Palacios et al., 2013) software to solve the smooth airfoil CFD fully-turbulence testcases in this thesis. This model defines the term ν_t as follows (Blazek, 2015):

$$\nu_t = \hat{\nu} f_{v1} \quad X = \frac{\hat{\nu}}{\nu} \tag{2.6}$$

$$\begin{aligned} \frac{\partial \tilde{\nu}}{\partial t} + \frac{\partial}{\partial x_j}(\tilde{\nu} v_j) &= c_{b1}(1 - f_{t1})\tilde{S}\hat{\nu} + \frac{1}{\sigma}\left[\frac{\partial}{\partial x_j}(\nu + \hat{\nu})\frac{\partial \hat{\nu}}{\partial x_j} + c_{b2}\frac{\partial \hat{\nu}}{\partial x_i}\frac{\partial \hat{\nu}}{\partial x_j}\right] \\ &\quad - \left[c_{\omega 1} f_\omega - \frac{c_{b1}}{\kappa^2} f_{t1}\right](\frac{\hat{\nu}}{d})^2 \end{aligned} \tag{2.7}$$

where d is the distance from the wall, $\tilde{S} = f_{v3}S + \frac{\hat{\nu}}{\kappa^2 d^2} f_{v2}$, the magnitude of the mean rotation rate $S = \sqrt{2 \times \Omega_{ij}\,\Omega_{ij}}$, rotation rate tensor $\Omega_{ij} = \frac{1}{2}(\partial v_i \partial x_j - \frac{\partial v_j}{\partial x_i})$ is the fluid vorticity$f_{v1} = \frac{X^3}{X^3 + C_{v1}^3}$, $f_{v2} = (1 + \frac{X}{C_{v2}})^{-3}$, $f_{v3} = \frac{(1+Xf_{v1})(1-f_{v2})}{\max(X,0.001)}$, $f_{\omega} = g\left[\frac{1+c_{\omega 3}^6}{g^6 + c_{\omega 3}^6}\right]^{1/6}$, $g = r + c_{\omega 2}(r^6 - r)$, $r = \frac{\hat{\nu}}{\tilde{S}\kappa^2 d^2}$,and $f_{t1} = C_{t1}\exp(-C_{t2}X^2)$. The constants values are $c_{b1} = 0.135$, $c_{b2} = 0.622$, $c_{v1} = 7.1$, $c_{v2} = 5$ $\sigma = \frac{2}{3}$,$\kappa = 0.41$, $c_{\omega 1} = \frac{c_{b1}}{\kappa^2} + \frac{1+c_{b2}}{\sigma}$, $c_{\omega 2} = 0.3$, $c_{\omega 3} = 2$, $c_{v1} = 7.1$, $C_{t1} = 1.3$, $C_{t1} = 0.5$, and $\nu = \frac{\mu}{\rho}$.

Based on the Sutherland law, the dynamic viscosity is calculated as:

$$\mu = \frac{1.45 \times 10^{-6} T^{3/2}}{T + 110} \tag{2.8}$$

where the temperature T is in degree Kelvin (k).

2.2.3 Extension to the Spalart-Allmaras model to account for the roughness

Aupoix and Spalart (Aupoix & Spalart, 2003) validated two extensions to the Spalart-Allmaras turbulence model to account for the roughness. Instead of discretizing the roughness elements, Boeing and ONERA models linked the actual roughness geometry to an idealized roughness on the wall, the equivalent sand grain roughness. With the validation of the two models with the MSU experiments, it was found that the friction coefficient could be predicted by these models. The model that is used in this thesis is based on the Boeing extension which increases the wall distance as indicated in Equation (2.9).

$$d_{new} = d + 0.03h_s \tag{2.9}$$

where d is the distance to the wall and h_s is the equivalent sand grain roughness. The latter h_s, is selected such that the shear stress at the wall is equivalent to the one above the real roughness geometries. Therefore the d_{new} replace the Spalart-Allmaras original distance from the wall. Thus:

$$X = \frac{\hat{\nu}}{\nu} + c_{R1}\frac{h_s}{d_{new}} \tag{2.10}$$

$$f_{v2} = 1 - \frac{X}{1 + Xf_{v1}} \tag{2.11}$$

where $c_{R1} = 0.5$. And the turbulence viscosity at the wall is not zero with the roughness model, the new $\hat{\nu}$ is calculated as (Aupoix & Spalart, 2003):

$$(\frac{\partial \hat{\nu}}{\partial n})_w = \frac{\hat{\nu}_w}{0.03h_s} \tag{2.12}$$

The model introduced could predict the shear stress at the wall. But additional thermal model is needed to predict the heat transfer above roughness. In this thesis, the thermal correction for the fully rough surface based on the model introduced by (Dipprey & Sabersky, 1963) and developed by (Morency & Beaugendre, 2020) is used to predict the heat transfer over the rough wall.

2.2.4 Prandtl correction model

Upon the validation of the Spalart-Allmaras model with modification for roughness, it was found that the heat transfer is overestimated over the surface with the constant equivalent sand grain roughness model (Morency & Beaugendre, 2020). Therefore, the 2PP model was introduced to take into the account another parameter, the roughness height to increase locally the turbulent Prandtl number. Figure 2.3 shows a close view of roughness height h above a wall. Below a certain height, in the melt down region, the flow is trapped, and recirculation

occurs. In the flow between the roughness elements, the proposed model reduces the turbulent heat transfer from the wall and increases the turbulent Prandtl, Pr_t . The increase in Prandtl number, ΔPr_t , should be a smooth function of y. It goes from its maximum value at the wall to the free stream value Pr_t above the roughness.

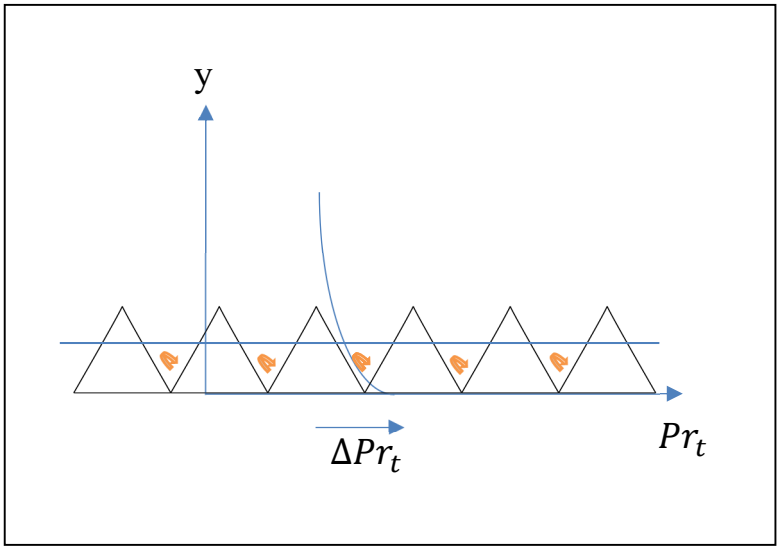

Figure 2.3 Roughness above the wall
Taken from (Morency & Beaugendre, 2020)

The main assumption is that the individual roughness geometries do not need to be discretized. The heat flux at the wall, q_w, is proportional to the temperature gradient in the normal direction.

$$q_w = k_{eff}(\frac{\partial T}{\partial n})_{wall} \tag{2.13}$$

For turbulent flows, the effective thermal conductivity $k_{eff}$is related to the laminar viscosity μ and the turbulent viscosity μ_{tur}(Morency & Beaugendre, 2020):

$$k = \frac{c_p \mu}{Pr} \tag{2.14}$$

$$c_p = \frac{\gamma R}{\gamma - 1} \tag{2.15}$$

$$k_t = \frac{c_p \mu_{tur}}{Pr_t^{eff}} \tag{2.16}$$

$$k_{eff} = k + k_t \tag{2.17}$$

In Equation (2.15) c_p is the specific heat at constant temperature and depends on fluid properties. The usual assumption for a turbulent flow is that the turbulent Prandtl number is constant, $Pr_t = 0.9$. For a smooth wall, the turbulent viscosity at the wall $\mu_{tur} = 0$. For a rough wall however, the turbulent viscosity is greater than 0 in the case of the extended Spalart-Allmaras turbulence model. To reduce the computed wall heat flux, the turbulent Prandtl number is increased near the rough wall by a value, which is a function of the rough wall distance and the roughness element shape (Morency & Beaugendre, 2020):

$$Pr_t^{eff} = Pr_t + \Delta Pr_t \tag{2.18}$$

$$\Delta Pr_t = FG\left(\frac{y}{h}\right) \tag{2.19}$$

$$G = exp\left(-\frac{y}{h}\right) \tag{2.20}$$

where F and G are two functions. In the case of the 2PP model used for this test case(Morency & Beaugendre, 2020),

$$F = 0.136\frac{gRe_s^{\alpha}Pr^{\beta}}{C} \tag{2.21}$$

$$Re_s = \frac{u_\tau h_s}{\vartheta} \tag{2.22}$$

where Re_s is the roughness Reynolds number. It defines the roughness region of the flow, which is a function of the shear velocity at the wall u_τ. The constant default values are C = 1.92, α = 0.45, and β = 0.8 (Morency & Beaugendre, 2020). In Equation (2.22) the shear velocity is selected such that the value is calculated above the roughness elements and computed based on Equation (2.23), with the corrected wall distance at the wall.

$$u_\tau = \frac{\tilde{\nu}}{\kappa(d + 0.03h_s)} \tag{2.23}$$

In Equation (2.23), $\tilde{\nu}$ is the kinematic viscosity of the fluid measured in the farfield. (Kays, 2012) suggested the following values for g :

$$\begin{gathered} g = 1 \quad if \quad Re_s \geq 70 \\ g = \frac{\ln Re_s - \ln 5}{\ln 70 - \ln 5} \quad if \quad 5 < Re_s < 70 \\ g = 0 \quad if \quad Re_s \leq 5 \end{gathered} \tag{2.24}$$

2.3 Post-calculation analysis

2.3.1 GCI method

The method used to study the effect of the mesh density on the solution is called the Grid Convergence Index (GCI). This method is commonly used to check the linear behavior of the meshes with increasing mesh densities. (Roache, 1994) proposed the GCI method to resolve

the quantification of uncertainty in the CFD studies using absolute values. The first step would be to calculate the order of convergence "p" using a constant grid refinement ratio " $r = 1.41$ " assuming the parameter on the finest grid is f_1:

$$p = \ln(\frac{f_3 - f_2}{f_2 - f_1}) / \ln r \tag{2.25}$$

where $f_1, f_2 \; and \; f_3$ are the three parameter values from Coarse, Medium and Fine meshes. It is used for the calculation of the Richardson Extrapolation to obtain the true value of the f parameter. In Equation (2.26), the value of $F_s = 1.25$. It is a safety factor for the evaluation of the GCI for the three mesh densities (Beisbart & Saam, 2019).

$$GCI = \frac{F_s \; |f_2 - f_1|}{r^p - 1} \tag{2.26}$$

2.3.2 Analyzed quantities

In this section, the quantities that are used to derive the correlations are introduced. These quantities are divided into the aerodynamics coefficients and the convective heat transfer coefficient which is the Nusselt number.

2.3.2.1 The lift coefficient and the drag coefficient

The lift coefficient and the drag coefficient are two coefficients that measure the aerodynamic forces over the airfoil using shear forces and the pressure distribution. Equations (2.27) and (2.28) are the definition of the lift and drag coefficient based on the lift and drag force over the airfoil.

$$C_L = \frac{L}{\frac{1}{2}\rho_\infty c V_\infty} \tag{2.27}$$

$$C_D = \frac{D}{\frac{1}{2}\rho_\infty c V_\infty} \tag{2.28}$$

In the two equations above, L and D are the drag and lift forces. They are calculated using the integration of the pressure and shear forces on the airfoil surface. c is the chord length. In the SU2 software, ρ_∞ and V_∞ , the density and the velocity at the farfield, are calculated as follows:

$$V_\infty = Ma\sqrt{\gamma R T_\infty} \tag{2.29}$$

where Ma is the Mach number, T_∞ is the farfield temperature and they are directly defined in the configuration file. For air, the heat capacity ratio is $\gamma = 1.4$ and the gas constant is $R = 287.058\ J/Kg\ K$. The ρ_∞ is calculated using the following equation (Anderson, 2011):

$$\rho_\infty = \frac{Re_c \mu}{V_\infty c} \tag{2.30}$$

where Re_c is the Reynolds number and defined as:

$$Re_c = \frac{\rho_\infty V_\infty c}{\mu} \tag{2.31}$$

Equation (2.31) indicates the Reynolds number, as a function of the density, chord length, velocity, and the dynamic viscosity.

2.3.2.2 Heat transfer and Nusselt number

The Nusselt number is the dimensionless number used for the convective heat transfer. For an airfoil, with a chord length, c, a thermal conductivity, k, and an average heat transfer coefficient h_{avg}, the average Nusselt number is defined as follow:

$$Nu_{avg} = \frac{h_{avg}\, c}{k} \tag{2.32}$$

The average heat transfer coefficient along the airfoil is:

$$h_{avg} = \frac{\oint h_s d_s}{2c} \tag{2.33}$$

The local heat transfer coefficient, h_s, is calculated using the local wall temperature T_s and the recovery temperature T_{total}:

$$h_s = \frac{q_w}{(T_s - T_{total})} \tag{2.34}$$

$$T_{total} = T_{\infty}\left(1 + r\frac{\gamma - 1}{2}Ma^2\right) \tag{2.35}$$

The local heat transfer coefficient is a function of the heat flux q_w which is calculated with the Equation (2.13) for the rough surface and Equation (2.36) for the smooth surface.

$$q_w = k(\frac{\partial T}{\partial n})_{wall} \tag{2.36}$$

For the verification of the results for the average Nusselt number the correlation of the average Nusselt number with the average Frossling number is used as per Equation (2.37).

$$Fr_{avg} = \frac{Nu_{avg}}{\sqrt{Re}} \tag{2.37}$$

2.3.2.3 Proposed form of the drag coefficient correlation for the airfoil

Correlations that describe the lift coefficient and the drag coefficient over airfoils and wings exist in the literature. For instance, (Hoerner, 1965) studied the correlation between the drag coefficient and the lift coefficient for a constant AOA at various high Reynolds numbers. He proposed a correlation for the increase of the drag based on the lift coefficient with a constant k:

$$\frac{\Delta C_D}{C_{Dmin}} = kC_L^2 \tag{2.38}$$

(Gudmundsson, 2013) presented a three-dimensional wing and two-dimensional airfoil drag correlation based on the lift coefficient. These correlations were derived using the curve fitting method based on CFD results. The two-dimensional correlation of drag and lift coefficient is given as follows:

$$C_D = C_{Dmin} + m.(C_L - C_{L_{minD}})^2 \tag{2.39}$$

In Equation (2.39), $C_{D_{min}}$ is the minimum drag coefficient, $C_{L_{minD}}$ is the lift coefficient where the drag is minimized and m is a coefficient indicating the parasitic drag increase of the airfoil, obtained from its drag polar. To obtain a good quality correlation, it is necessary to ensure that the analysis consist of the results before the maximum lift coefficient (C_{Lmax}). We could see from the literature that the correlations between the drag coefficient and lift coefficient is a quadratic equation. However, because of the limitation of the quadratic equation at the high angles of attack, Gudmundsson suggested a quartic equation near the stall angle. Therefore, to have a well-estimated result and increase the range of the validity, a new correlation is suggested based on the lift coefficient as in Equation (2.40).

$$C_D = C_{Dmin} + k_1 C_L^2 + k_2 C_L^4 \tag{2.40}$$

In the presented form, the hypothesis is that the lift coefficient is zero at the minimum drag for a symmetric airfoil ($C_{LminD} = 0$).

2.3.2.4 Proposed form of the average Nusselt number correlation on the airfoil

The Nusselt number is defined as the ratio of the convective heat transfer over the conductive heat transfer. It depends on the convective heat transfer coefficient and the thermal conductivity as defined in Equation (2.32) for an airfoil. (Wang et al., 2008) conducted a series of experiments over the NACA0012 airfoil at different AOA. The experimental setup included 25 thermocouples inside and outside of the airfoil. They measured the heat flux between the heated internal and cooled external airfoil. With the temperature and the heat flux measurements, they calculated the heat transfer on the surface of the airfoil. The correlations of Wang based on the Nusselt number, the AOA and the Reynolds number are as follows:

$$\overline{Nu} = 0.0943(0.75 + 0.017\alpha\ ){Re_c}^{0.636}Pr^{\frac{1}{3}} \quad for\ Re_c > 5 \times 10^5 \tag{2.41}$$

$$\overline{Nu} = 2.482(0.75 + 0.013\alpha\ ){Re_c}^{0.389}Pr^{\frac{1}{3}} \quad for\ Re_c \leq 5 \times 10^5 \tag{2.42}$$

For turbulent flows over the smooth NACA0012 airfoil, Samad (Samad, 2021) proposed, based on the numerical results, a correlation using the average Frossling number, the Reynolds number, the Prandtl number and the AOA as the format of Equation (2.43) for a zero angle of attack and shown by Equation (2.44) for $0^{\circ} < AOA < 16^{\circ}$.

$$Fr_{avg}(\alpha = 0) = 0.020{Re_c}^{0.335}Pr^{\frac{1}{3}} \tag{2.43}$$

$$Fr_{avg} = 0.020\ (1 + 1.131\alpha - 8.634\alpha^2 + 10\alpha^3){Re_c}^{0.335}Pr^{\frac{1}{3}} \tag{2.44}$$

A new correlation in this thesis is sought between the average Nusselt number and the lift coefficient. The proposed equation is suggested in a way that the average Nusselt number

would be better predicted on an airfoil with a quartic variation of the lift coefficient in the form of Equation (2.45).

$$\overline{Nu} = \overline{Nu}_{max} + k_1 C_L^2 + k_2 C_L^4 \tag{2.45}$$

As can be seen in the experimental measurements of the heat transfer near the stagnation point of an airfoil in a flowfield, the increase of roughness results in increasing heat transfer (Poinsatte et al., 1991). Therefore, it is expected that for rough surfaces, the $\overline{Nu}_{max}$ value is higher in the rough case study compared to the smooth surface.

2.4 Numerical method

The Finite Volume Method (FVM) is used by SU2 for the element discretization using unstructured meshes in the computational domain. An integrated numerical method of SU2 could be found in the work of (Molina et al., 2017). SU2 uses median-dual vertex-based scheme to build the control volumes which is indicated in Figure 2.4. The figure shows the discretization in the SU2 which uses an unstructured based method connecting the cell centered of the domain to make the control volumes indicated by Ω_i.

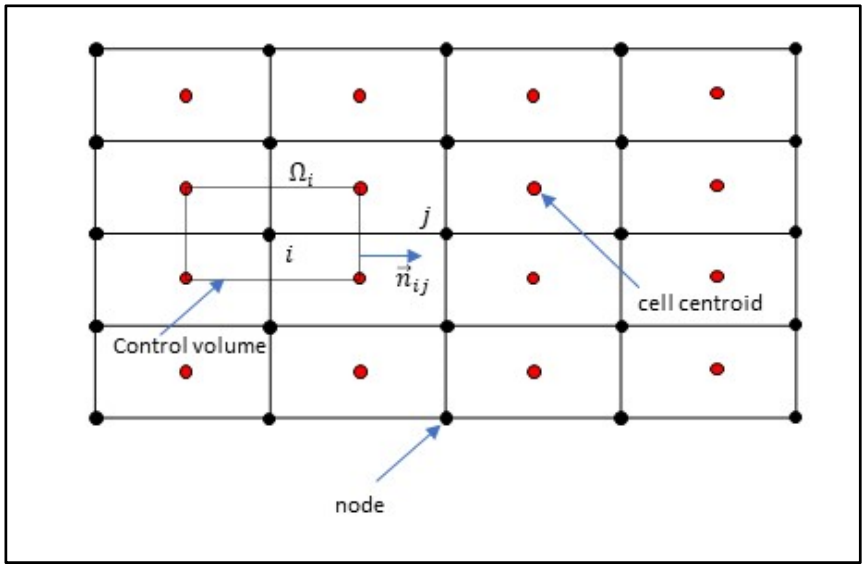

Figure 2.4 SU2 2-D discretization

Therefore, the governing equations in the Partial Differential Equations (PDE's) form are integrated as per Equation (2.46) (Molina et al., 2017):

$$\int_{\Omega_i} \frac{\partial U}{\partial t} d\Omega + \sum_{j \epsilon \mathcal{N}(i)} (\tilde{F}_{cij} + \tilde{F}_{vij}) \Delta S_{ij} - Q|\Omega_i| = \int_{\Omega_i} \frac{\partial U}{\partial t} d\Omega + R_i(U) = 0 \qquad (2.46)$$

where $\tilde{F}_{cij}$ and $\tilde{F}_{vij}$ are the projected numerical approximation for the convective and viscous fluxes and calculated at the middle of the edges. Q is the source term, ΔS_{ij} is the area of the face associated with the cells i and j edge, Ω_i is the control volume and $\mathcal{N}(i)$ is the nodes neighbor to the node i. The convective fluxes are computed using the SLAU2 scheme (Kitamura & Shima, 2013) with the second order upwind reconstruction and Venkatakrishnan limiter. For the turbulent variables for the SA and SA_ROUGH models, the convective fluxes are computed using the second-order scalar upwind method. The FGMRES linear solver is used to solve the linearized system of equations. The Green-Gauss gradient scheme is used for the viscous flux approximation in this problem.

2.4.1 Computational domain

The overall numerical domain is illustrated in the Figure 2.5. The airfoil with the chord length of c=1m is placed at the center of the calculation domain. The leading edge is placed at x=0 and y=0. The boundary of the domain is set at 100c from the cord. The airfoil has the wall boundary condition with a constant temperature and the circle is the farfield boundary condition.

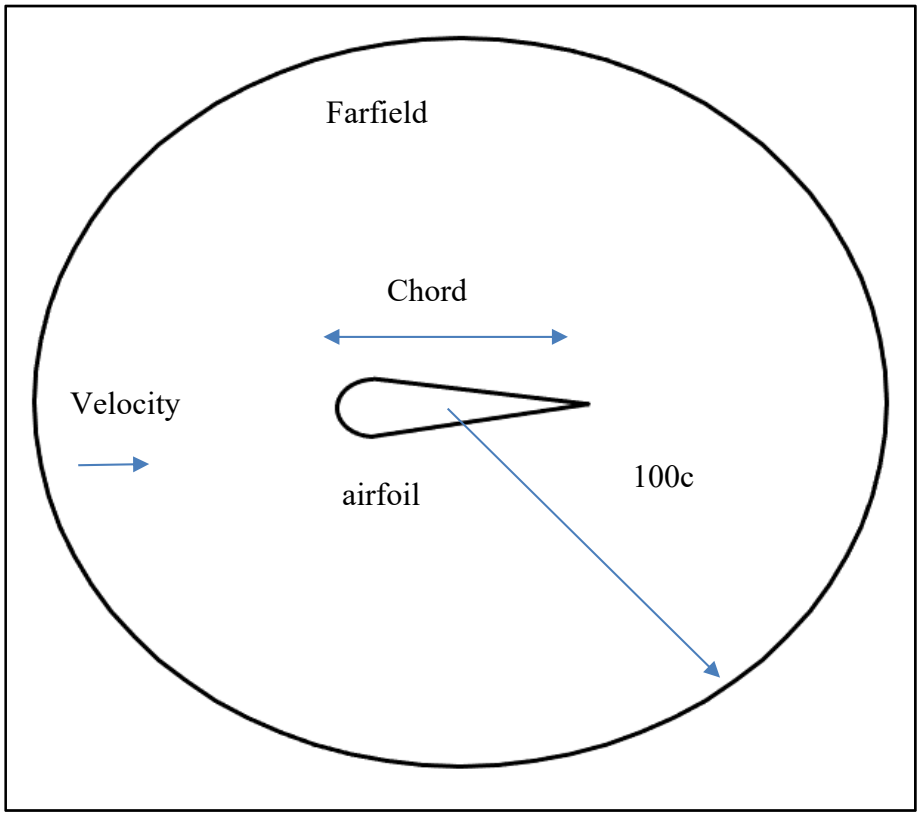

Figure 2.5 Scheme of the numerical domain

2.5 Boundary condition

In this problem, the initial and Boundary Condition (BC) is defined based on (Blazek, 2015). In SU2 software, the initial condition is defined at time $t = 0$. The boundary condition is an artificial boundary in which, the values for the physical quantities are defined. In this section, the inlet, outlet, and farfield boundary conditions are discussed.

For the initial condition, the values for the Mach number, the static temperature, and the Reynolds number are directly defined in the SU2 configuration file. Using Equation (2.29), the value of the freestream velocity is calculated. The density is defined using the dynamic viscosity, calculated with the Sutherland law, and Reynolds number. The total pressure is defined as the initial BC and calculated as follows:

$$P_{total} = P_{\infty}\left(1 + r\frac{\gamma - 1}{2}Ma^2\right)^{\frac{\gamma}{\gamma - 1}} \tag{2.47}$$

The numerical calculations in the CFD must be conducted in a bounded domain. For this reason, the farfield boundary condition is defined with the freestream values at the distance of "$100 \times c$" from the airfoil. In most of the heat transfer problems in CFD, an imposed temperature or heat flux is considered over the wall boundaries of the domain. In this problem, the airfoil wall boundary condition has an imposed constant temperature of $300\ K$ and the farfield temperature is set to $288.15\ K$.

2.6 Summary

In this chapter, first the RANS equations were introduced. The RANS model was presented along with the Spalart-Allmaras turbulence model taking into account the roughness of the surface. Then, the GCI method used to evaluate the result uncertainties with the increase of the mesh density was given. For the rough surface model, the 2PP thermal model considers the roughness height of the surface to model the heat transfer on the wall. Following the selection of the mathematical models, the two suggested forms of correlations for the aerodynamic coefficient and the heat transfer coefficient were derived based on the previous works. The last part of this chapter presented the numerical method and the computational domain.

CHAPTER 3

NUMERICAL RESULTS AND ANALYSIS

Based on the methodology presented in chapter 2, the numerical results are shown in this chapter. First, the mesh is selected using the GCI method to ensure the good quality of the results. Then, the predicted heat transfer and aerodynamics coefficients are verified and validated before being used to build the database. With the database, the aerodynamic and heat transfer correlations are derived to estimate the drag coefficient and the average Nusselt number as a function of the lift coefficient.

The analysis uses streamlines and Mach contours for the smooth and the rough surface of the NACA 0012 airfoil so as to have a visual overview. Then, the CFD results of the NACA0009 airfoil are compared to previous works. Then, the NACA0012 results are verified and validated against experimental data for both smooth and rough surfaces. The aerodynamic coefficient for the NACA0015 is validated and verified for the smooth surface following the heat transfer verification and validation for the NACA0012 with the smooth surface. Then, the database is built with the results of the lift and drag coefficient and the average Nusselt number for the NACA0009, NACA0012, and NACA0015 airfoil for the four Reynold's numbers ($Re = 6.25 \times 10^5, 1.25 \times 10^6, 2.5 \times 10^6, and\ 5 \times 10^6$) with the smooth and rough surfaces. Finally, the correlations between the lift and drag coefficients and a novel Nu_{avg} correlation based on the lift coefficient are presented and the results are analysed.

3.1 Verification and validation

3.1.1 Meshes used for the GCI

In order to determine the mesh density to use in the CFD calculations, the Grid Convergence Method (GCI) (Roache, 1994) is applied for three mesh densities: coarse, medium, and fine.

The GCI is a method to evaluate the mesh dependence and estimate the numerical discretization error. The mesh properties used for this calculation are presented in Table 3-1 for the NACA0009 airfoil. The coarse, medium and fine densities of the mesh are generated with the GMSH software and the size of the elements are decreased by a factor of 1.41 in all of the directions between each mesh.

Table 3.1 Mesh properties for the coarse, medium and fine density mesh for the NACA0009 airfoil

Mesh size	Mesh element size ($airfoil \times farfield$)	Number of Vertices (points)	Number of Elements	y plus
Coarse	401×130	121631	207965	0.48
Medium	566×181	208471	367663	0.35
Fine	788×253	366526	662542	0.25

The coarse mesh is used for visualizing and showing the overall computational domain, the mesh around the airfoil, and the trailing and leading edge in Figures (3.1), (3.2), and (3.3). The mesh density is increased downstream in the wake region compared to the front part of the calculation domain.

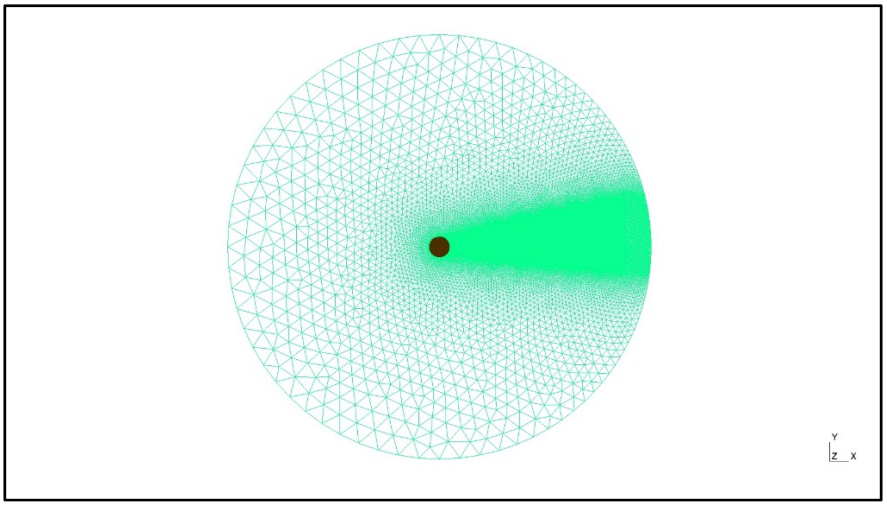

Figure 3.1 Overall mesh view within the computational domain

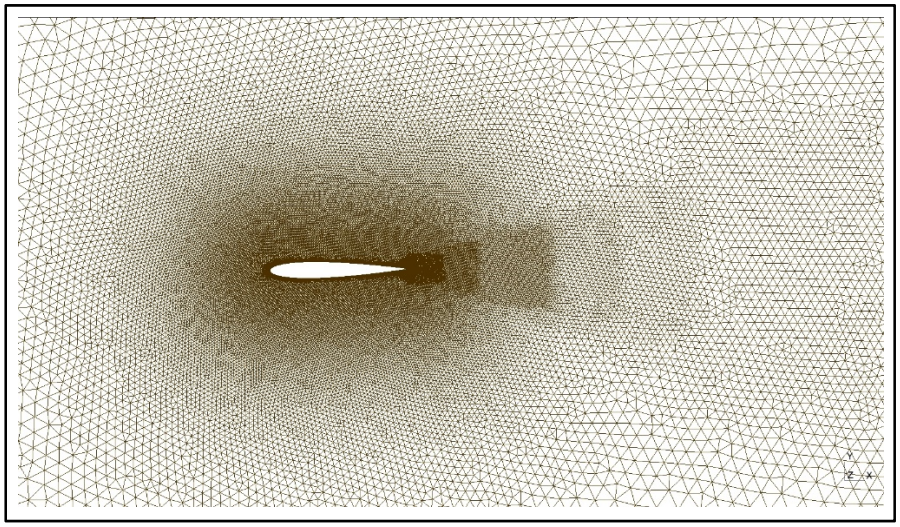

Figure 3.2 The overall view of the mesh around the airfoil

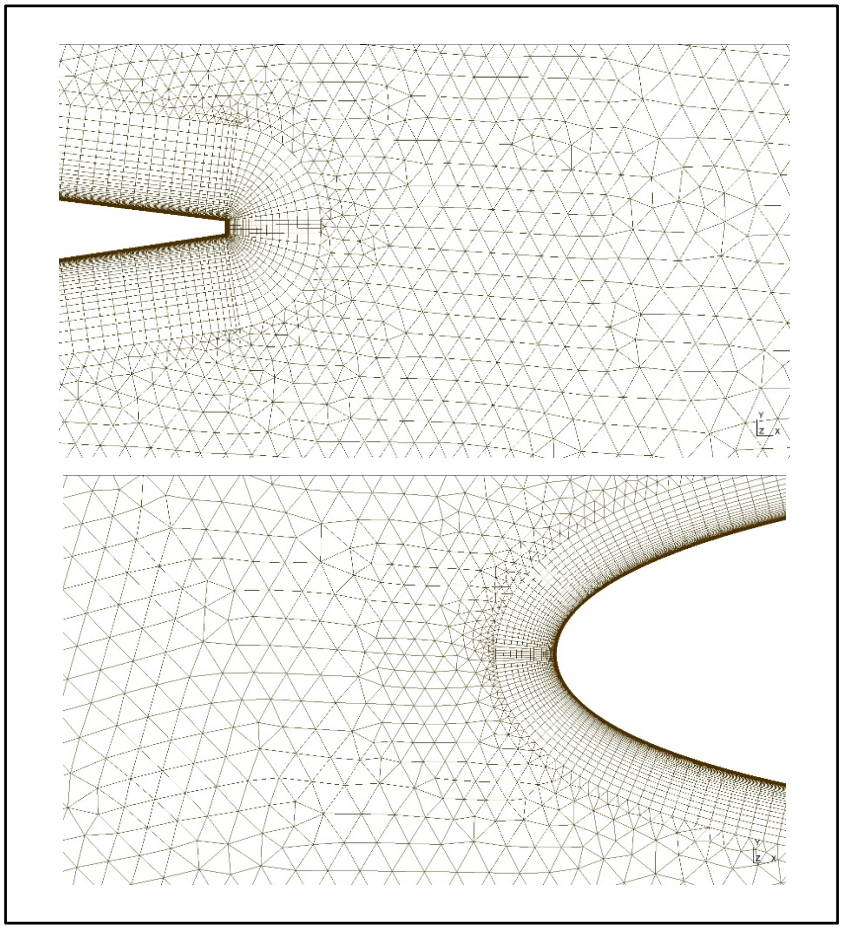

Figure 3.3 Mesh elements distribution over the leading edge and the trailing edge

The coarse mesh for the NACA 0009 testcase has 121631 points (nodes) and 207965 calculation elements. The mesh elements contain two types of elements: triangular elements distant from the airfoil and quadrilateral elements close to the airfoil which are shown in Figure 3.3.

3.1.2 GCI calculation

To select the mesh, the lift coefficient, the drag coefficient, and the Nusselt number results for the three mesh densities are calculated. Table 3-2 shows the fine mesh GCI results for the lift, the drag and the average Nusselt for the three NACA0009, NACA0012 and NACA0015 airfoils for the rough and smooth surfaces with the coarse, medium, and fine mesh densities

assuming the theoretical order of the method to be $p = 2$ in Equation (2.26). From the total of 54 testcases, in 8 occurrences, the GCI has a value over 1% and in four occurrences have a value over 2%. For the lift coefficient and the average Nusselt, the average GCI for the rough surfaces is higher than for the smooth surface but for the drag coefficient, the smooth surfaces have the higher average GCI value in comparison to the rough surface.

Table 3.2 GCI value for the three mesh densities for the NACA0009, NACA0012, and NACA0015 smooth and rough airfoils

Airfoil		**AOA**	**Lift coefficient**	**Drag coefficient**	**Nusselt number**
			GCI %	GCI %	GCI %
NACA0012	Smooth	0	0.05	0.57	0.14
		10	0.13	1.31	0.18
		15	0.4	1.99	0.07
NACA0015		0	0.02	0.79	0.14
		10	0.04	0.3	0.17
		15	0.22	0.46	0.16
NACA0009		0	0.02	0.43	0.12
		10	0.21	2.32	0.05
		13	0.36	3.06	0.14
NACA0012	Rough	0	0.01	0.2	0.2
		5	0.22	0.13	0.4
		8	0.03	0.12	0.53
NACA0015		0	0.33	0.14	1.62
		5	0.41	0	2.43
		8	0.13	0.41	2.47
NACA0009		0	0.12	0.14	0.72
		5	0.009	0.16	0.94
		8	0.3	0.11	1.022

Regarding the GCI results, the fine mesh density is selected in the following to derive the heat transfer and aerodynamics correlations. An overall look at the GCI results shows that 14% of the results have the GCI value over 1 %. .

3.1.3 Angle of attack and the maximum lift coefficient

Because of the RANS model limitations, this study focuses on the aerodynamic and heat transfer coefficient up to the stall angle. Therefore, in this section, the AOA at the highest lift coefficient is studied for the NACA0009, NACA0012, and NACA0015 with the smooth and rough surfaces at the lowest testcases Reynolds number. The results are used next to derive the correlation between the drag and lift coefficient and the Nusselt and the lift coefficient. The AOA of the maximum lift coefficient at the Reynolds$= 625000$ is presented in Table 3-3.

Table 3.3 Maximum AOA based on the lift coefficient for the three airfoils with the fine mesh density

		NACA 0012	NACA 0015	NACA 0009
AOA at C_{Lmax}	Smooth	15°	16°	$\underline{13^{\circ}}$
	Rough	11°	11°	$\underline{9^{\circ}}$

From Table 3-3, the stall angle is $AOA = 13^{\circ}$ for the smooth surface and $AOA = 9^{\circ}$ for the rough surface. The reason for choosing the lowest value between the results, is to have a single and valid AOA that would be applicable to derive the correlation. The AOA ranges are selected such that the testcases do not experience stall even with the lowest Reynolds number of the testcases ($Re = 625000$).

3.1.4 Mach and pressure iso contours:

In this section, the study of the pressure and Mach number distributions around the airfoil is conducted for the NACA 0012 with the $Re_c = 2.5 \times 10^6$ and the velocity of $Ma = 0.2$ in the freestream. Figure 3.4 shows the pressure distribution with the streamlines contour for the smooth and rough surfaces with the $AOA = 10^{\circ}$. The main noticeable difference is at the trailing edge where vortices are formed and separation is seen for the rough surface. The pressure distribution does not show a noticeable difference between the two results.

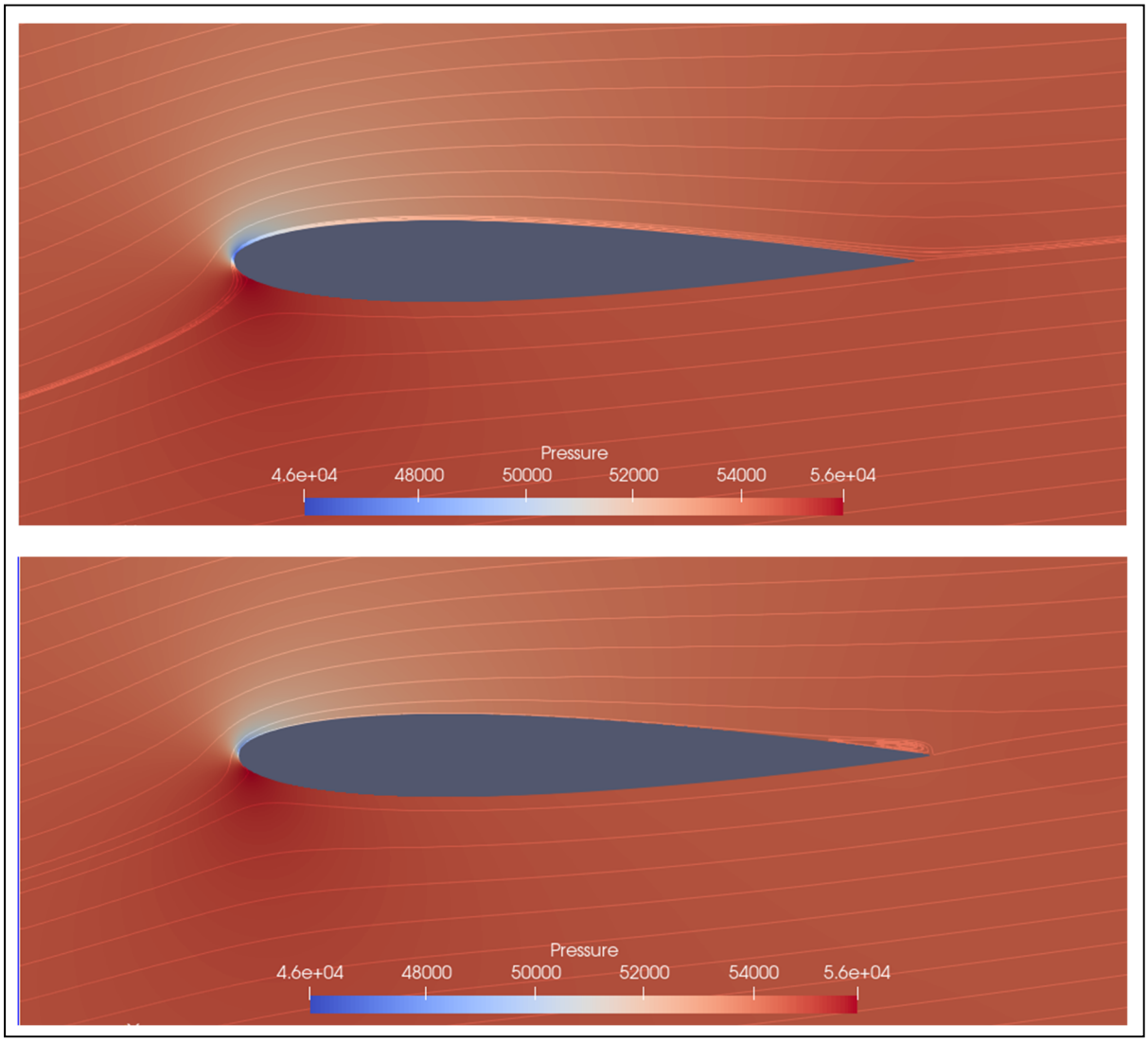

Figure 3.4 The pressure distributions and flow streamline for the smooth and rough NACA 0012 at the $AOA = 10^{\circ}$

Figure 3.5 shows the Mach iso contour for this testcase. In this figure, the overall Mach number is higher for the smooth surface than the rough surface. Also, the same observation can be made with Figure 3.4 that the separation is visible at the trailing edge of the airfoil, characterized by a zone of low Mach number outside of the boundary layer area.

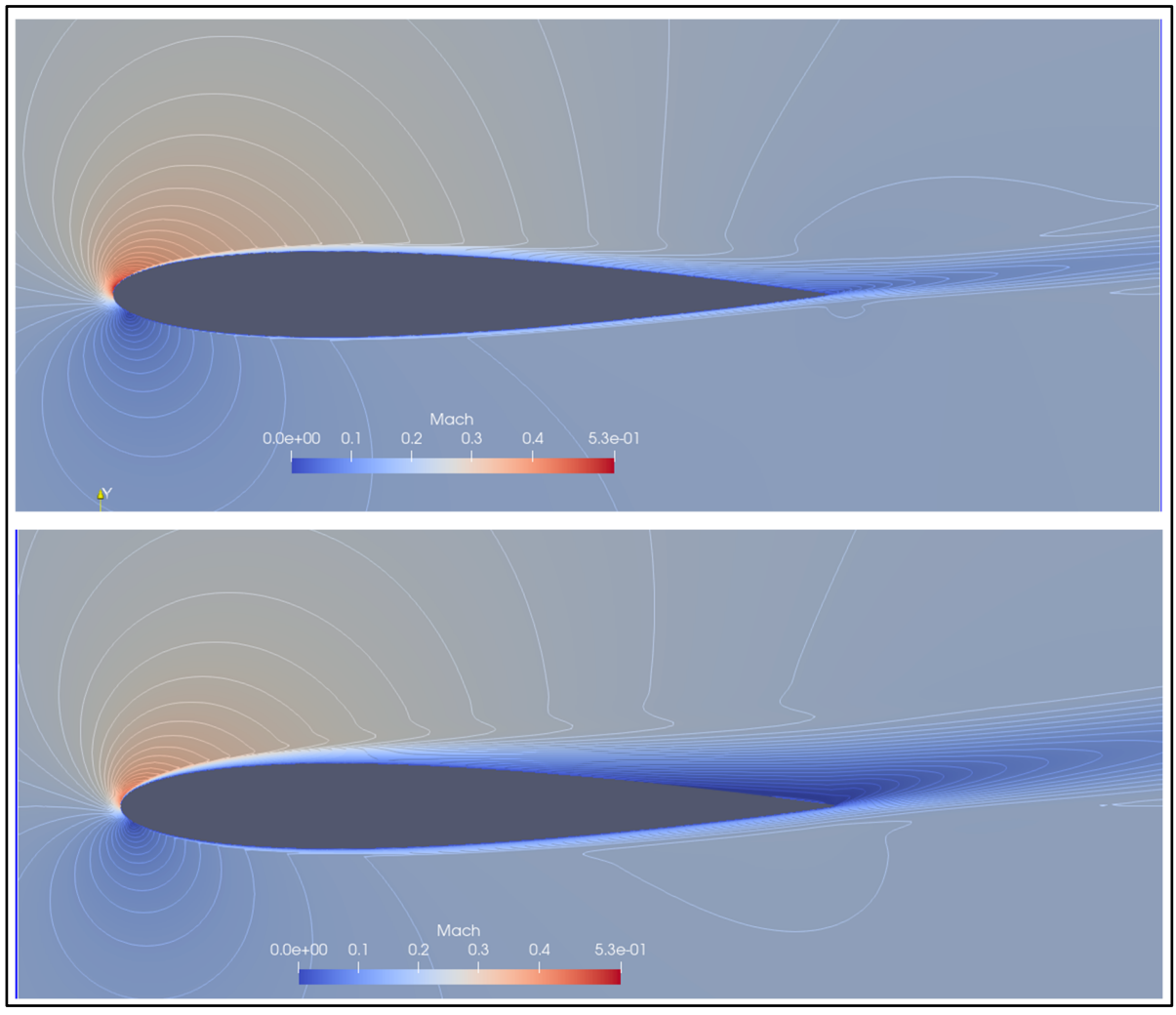

Figure 3.5 The Mach number iso contour for the smooth and rough NACA 0012 at the $AOA = 10^{\circ}$

3.1.5 Aerodynamic and heat transfer verification and validation

In this section, the results for the smooth and rough surfaces for the three airfoils are verified and validated. The Spalart-Allmaras turbulence model with and without the activated roughness on the airfoil are utilized in the simulation. To facilitate the identification of the model used in each section, the following nomenclature is used. In general RANS-SA is used for both rough and smooth surfaces CFD results. SA-SMOOTH is used for the RANS Spalart-Allmaras model and roughness is not activated. SA-ROUGH is used when the roughness is activated. The grid for both smooth and rough simulations are the same in the farfield boundary conditions.

At first, the CFD SA-SMOOTH results of the lift coefficient for the NACA0009, the NACA 0012, and the NACA0015 airfoils are compared. Then CFD SA-ROUGH result for the same airfoil is verified with previous work. For the heat transfer coefficient, the Fr_{avg} for the NACA0012 smooth airfoil is compared and the Nu_{avg} is validated against experiments.

3.1.5.1 Smooth NACA 0009

The aerodynamic CFD results of the smooth NACA0009 airfoil is compared against Xfoil prediction in this section. Xfoil is a program, developed by Drela and Giles in 1987 which uses a low-fidelity method to predict the aerodynamic coefficient for the range of Reynolds numbers, Mach numbers, and $-15^{\circ} \leq AOA \leq 15^{\circ}$ due to the stall angle (Drela, 1989).

For the comparison, the testcase has the following conditions: $Re_c = 1 \times 10^6$ and $0^{\circ} \leq AOA \leq 16^{\circ}$. To perform this analysis, the fine mesh density (788×253 ($elements\ number\ on\ the\ airfoil \times elements\ number\ in\ the\ farfield$) is used. Figure 3.6 shows the comparison of the NACA0009 airfoil SA-SMOOTH and the Xfoil CFD results. As shown, SA-SMOOTH could predict the lift coefficient at the low and high angles of attack near the stall angle. For the two numerical results, the stall happens at $AOA = 14^{\circ}$ with

a discrepancy of 2.2% on the highest lift coefficient prediction. However, the maximum error occurs at $AOA = 8^{\circ}$ with a 9.8% of discrepancy between the two results.

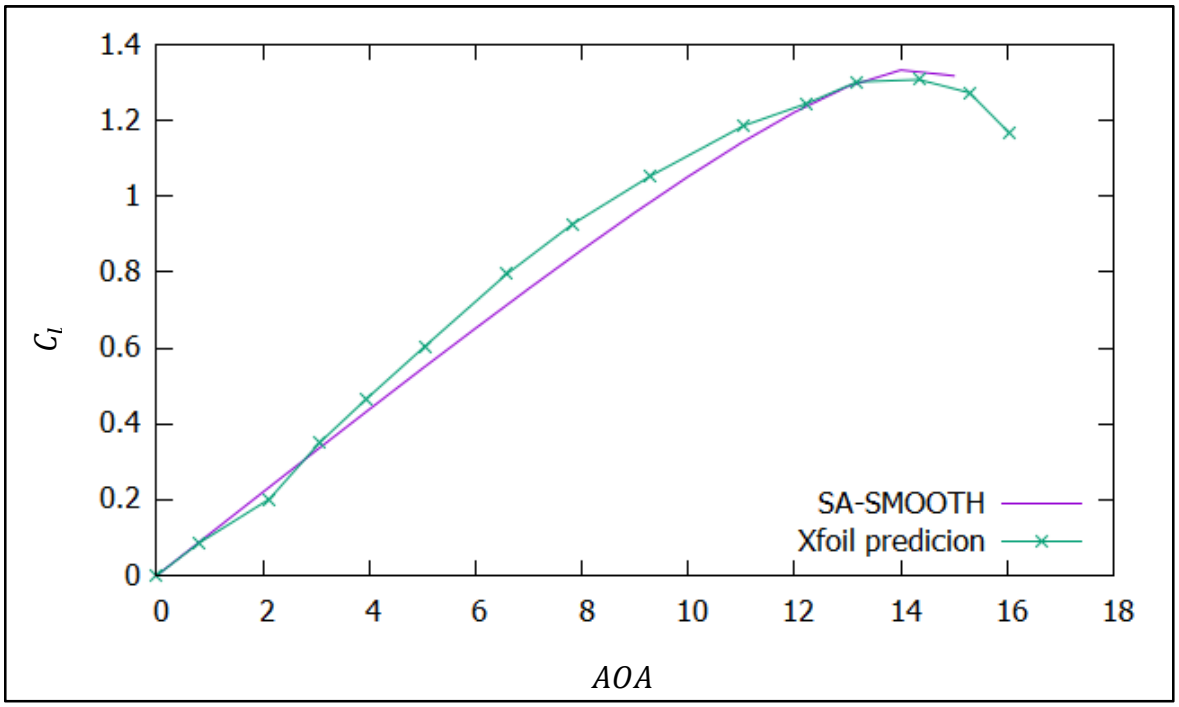

Figure 3.6 Verification for the NACA0009 smooth airfoil

3.1.5.2 Smooth and rough NACA0012

In this section, the RANS-SA estimation for the lift coefficient is evaluated and compared to the numerical results of (Tagawa, Morency, & Beaugendre, 2021), OVERFLOW (Jespersen, Pulliam, & Childs, 2016) and the experimental results of (Ladson, 1988). Both smooth and rough surfaces are compared in this section but the rough airfoil is just compared with the work of (Tagawa et al., 2021).

The validation and verification are conducted using a fine mesh density of $794 \times 253(elements\ number\ on\ the\ airfoil \times elements\ numberin\ the\ farfield)$. First, the

result of SA-SMOOTH is compared with the results of OVERFLOW CFD and the Ladson experiments. The physical boundary condition is $Ma = 0.15,\ Re_c = 6 \times 10^6$. However, for the validation, Ladson performed a variety of experiments for a range of Reynolds and Mach numbers. Therefore, the selected testcase for the validation of our CFD result is $Ma = 0.2,$ $Re = 6 \times 10^6$.

Figure 3.7 presents the lift coefficient variation at $-1^\circ < AOA < 19^\circ$ for the CFD SA-SMOOTH results with the Ladson experiments and OVERFLOW CFD results. For this testcase that is conducted with$Re_c = 6 \times 10^6,$ the AOA range is higher than the values showed in Table 3-2. As shown in the figure, the SA-SMOOTH result slightly overestimates the lift coefficient but the SA-SMOOTH predicts an $AOA = 17.9^\circ$ for the maximum lift coefficient while (Ladson, 1988) predicted $AOA = 17.3^\circ$ for the stall angle. The OVERFLOW results are well-predicted by SA-SMOOTH with a maximum discrepancy of below 1%.

Figure 3.8 presents the variation of the lift coefficient with the increase of the angle of attack for the rough NACA0012 airfoil. For the rough surface, (Tagawa, 2021) utilized the RANS-SA model using the one parameter equivalent sand grain roughness method for different equivalent sand grain roughness heights and Reynolds numbers for the NACA 0012 airfoil. The test case of $Ma = 0.15,\ h_s = 25 \times 10^{-4}$ is selected for the verification. The verification of SA-ROUGH CFD result shows a maximum discrepancy of 1.6% at the highest lift coefficient with Tagawa's results.

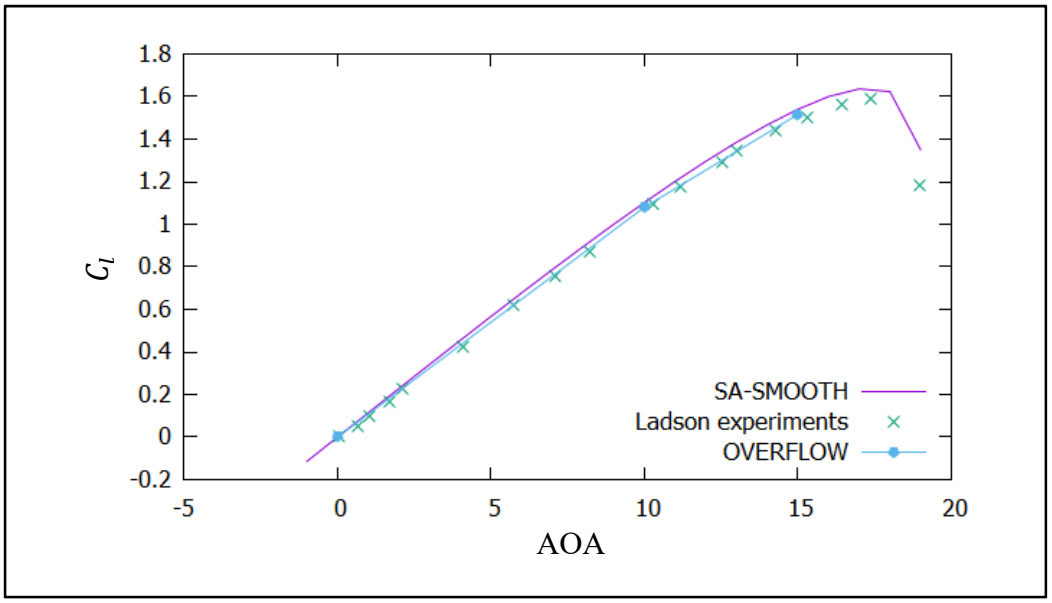

Figure 3.7 Lift coefficient verification and validation for the smooth NACA0012

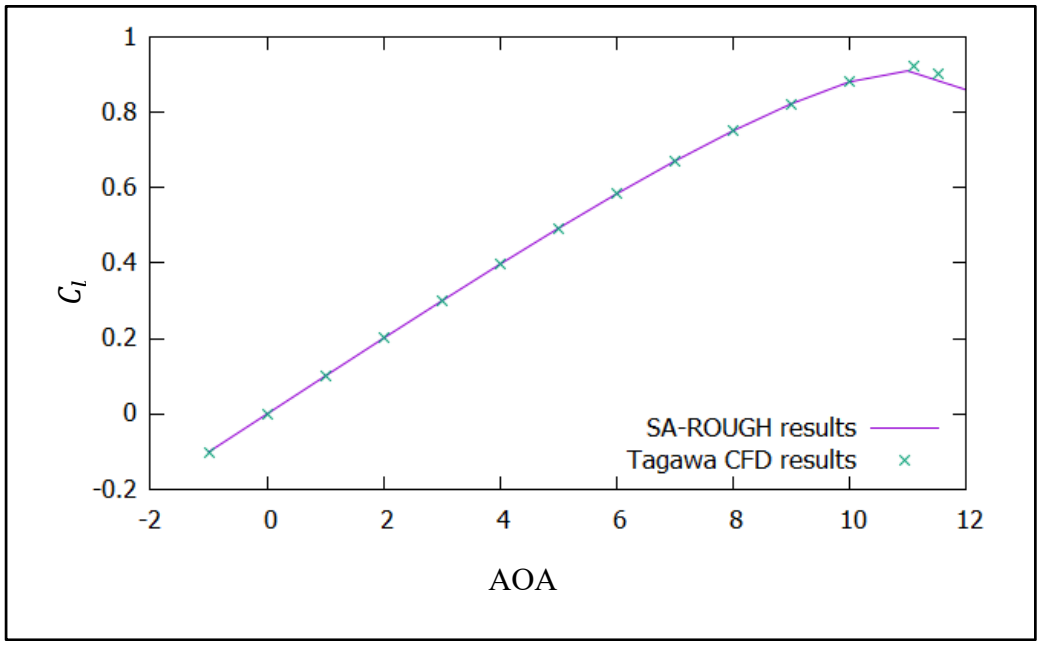

Figure 3.8 Lift coefficient verification for the rough NACA0012

3.1.5.3 Smooth NACA0015

In this section, the CFD results of the SA-SMOOTH is compared and validated. The analysis is conducted using the fine density mesh of 788×253 ($elements\ number\ on\ the\ airfoil \times elements\ number\ in\ the\ farfield$). The physical condition of the SA-SMOOTH testcase is $Ma = 0.15$ and $Re_c = 1.25 \times 10^6$. Results are compared with (Joslin, Horta, & Chen, 1999) which used the one equation Spalart-Allmaras turbulence model with $Ma = 0.15$ and $Re_c = 1.2 \times 10^6$ for the testcase. Also, the CFD result is validated with the experiments of (Bove, 2008) and retrieved from the work of (Gilling & Sørensen, 2008) with the physical condition of $Re_c = 1.6 \times 10^6$.

Figure 3.9 shows the variation of the lift coefficient with the angle of attack for the NACA0015 smooth airfoil. The stall angle for the two numerical results is about 16° and the maximum discrepancy between the two numerical results is 2.7% at $AOA = 10^{\circ}$. For the validation, between the experimental results and the two numerical results, the error is almost 13% at the stall angle. The reason for the error between the two numerical solutions and the experiment is related to the condition of the experimental test case as the Mach number is not mentioned and only the Reynolds number is available.

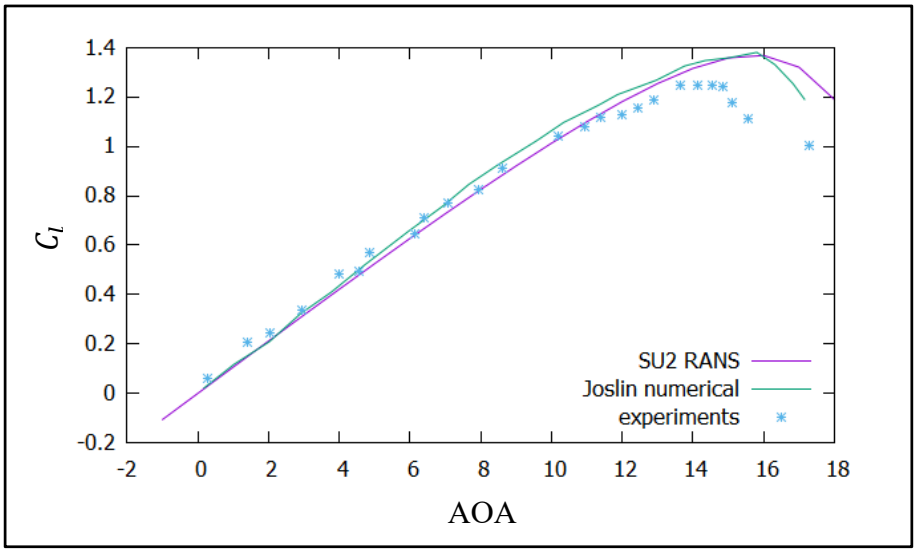

Figure 3.9 Lift coefficient validation and verification of the smooth NACA0015

3.1.5.4 Average Nusselt number

In this section, the results of the average Nusselt number for the NACA0012 airfoil are compared against the numerical work of (Samad, 2021) and the work of (Poinsatte et al., 1990) for the smooth airfoil. Results for the CFD comparison are for a $Re_c = 2.5 \times 10^6$ and $AOA = 0^\circ$ to $AOA = 16^\circ$ as per the work of (Samad, 2021). The average Nusselt number is selected for the comparison based on the relation between the average Nusselt number and the average Frossling number which is mentioned in Equation (2.37).

For the validation, the experimental results are extracted from the work of (Poinsatte et al., 1990). He conducted a series of experiments to measure the heat transfer at the leading edge of the NACA0012 for both smooth and rough surfaces. Therefore, the CFD results for the Nusselt number are compared at the stagnation point against his experiments.

Figure 3.10 presents the results of the Frossling number at $Re = 2.5 \times 10^6$ and $AOA = 0^\circ$ to $AOA = 16^\circ$. From the figure, the maximum error between the two results is 1.9% at the $AOA = 12^\circ$. Although the results of the heat transfer are slightly underestimated before the $AOA = 10^\circ$, it is overestimated after this point. Figure 3.11 presents the results of NASA experiments conducted by (Poinsatte et al., 1991) at the stagnation point for the NACA0012 smooth airfoil at $AOA = 0^\circ$ compared to the CFD calculation. The error is below 1% until a $Re = 2.5 \times 10^6$ and results are well estimated. Although a maximum error of 5.4% occurs at $Re = 3.5 \times 10^6$.

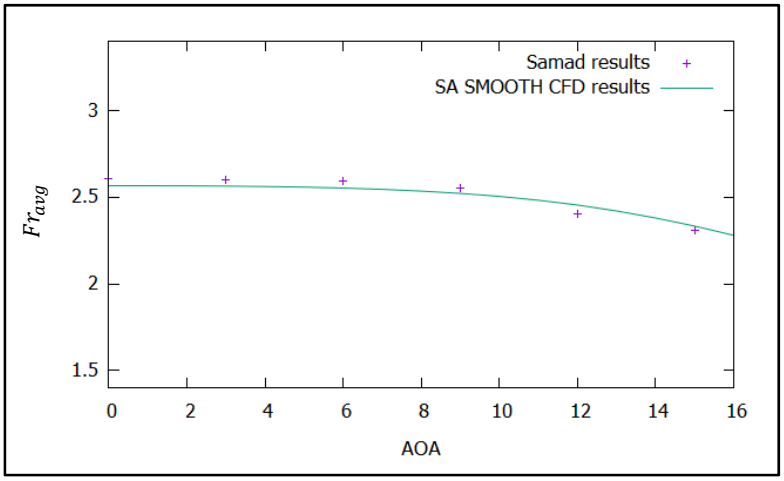

Figure 3.10 Verification of the average Frossling number for the NACA0012

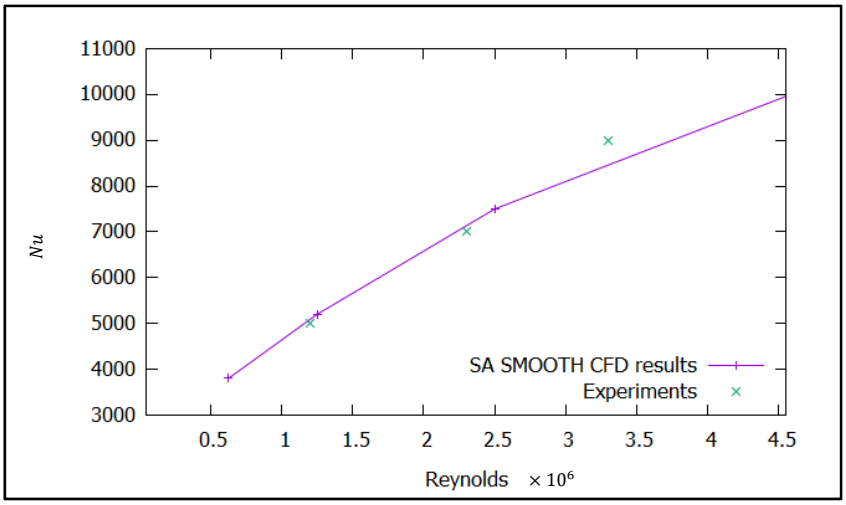

Figure 3.11 Validation of the local Nusselt number at the stagnation point for the NACA0012

3.1.6 Reynolds number effect on the heat transfer

In this section, the effect of the Reynolds number variation on the Nusselt number at two angles of attack, $AOA = 0^{\circ}$ and $AOA = 10^{\circ}$ is investigated for the NACA 0015, NACA 0012, and NACA 0009 airfoils.

Figure 3.12 and 3.13 show the variation of the local Nusselt number versus x/c on both sides of the NACA 0009, NACA 0012, and NACA0015 airfoils with the smooth surface. The first, second, and third sub-figures correspond to the NACA 0015, NACA 0012, and NACA 0009 airfoils respectively. Figure 3.12 shows the result at $AOA = 0^{\circ}$ while Figure 3.13 shows the result of $AOA = 10^{\circ}$. From the results, all airfoils experience a maximum heat transfer close to the leading edge of the airfoil excepted the testcase with the $Re = 5 \times 10^6$ for NACA 0015 airfoil. From the comparison of the two examined angles of attack, with the AOA increase, the local Nusselt number increases significantly close to the leading edge of the airfoil.

Using the thermal conductivity, k, and an average heat transfer coefficient h_{avg} over the airfoil, the Nusselt number is calculate for the three airfoils. As seen in Figure 3.12 and 3.13, with the increase of the Reynolds numbers, all the cases experience an increase of the local Nusselt number. Although the difference between the various Reynolds numbers is more significant for the $AOA = 0^{\circ}$ compared to the $AOA = 10^{\circ}$ for the three airfoils.

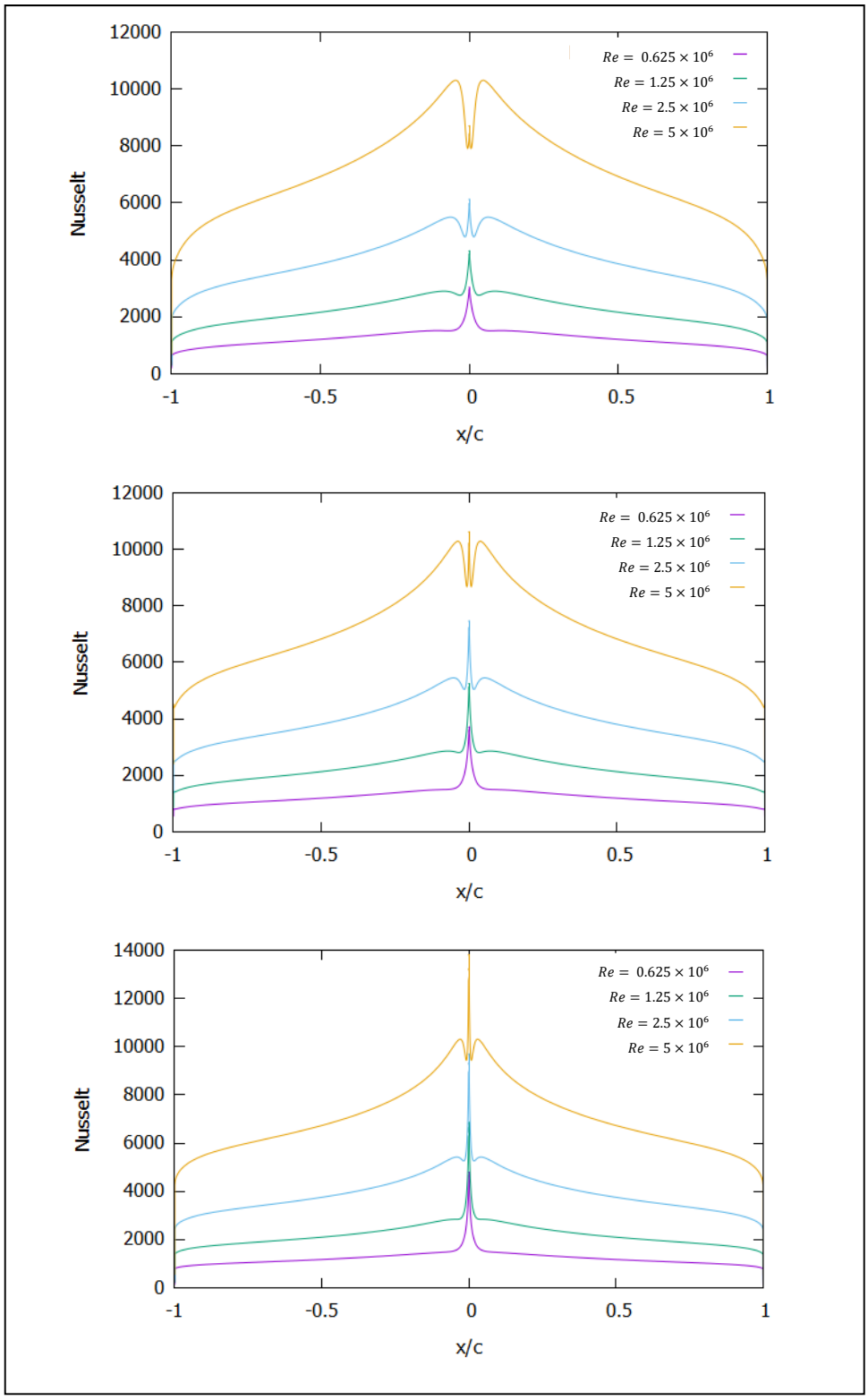

Figure 3.12 Local Nusselt number at the $AOA = 0^{\circ}$ for the NACA 0015, NACA 0012, and NACA 0009 smooth airfoils

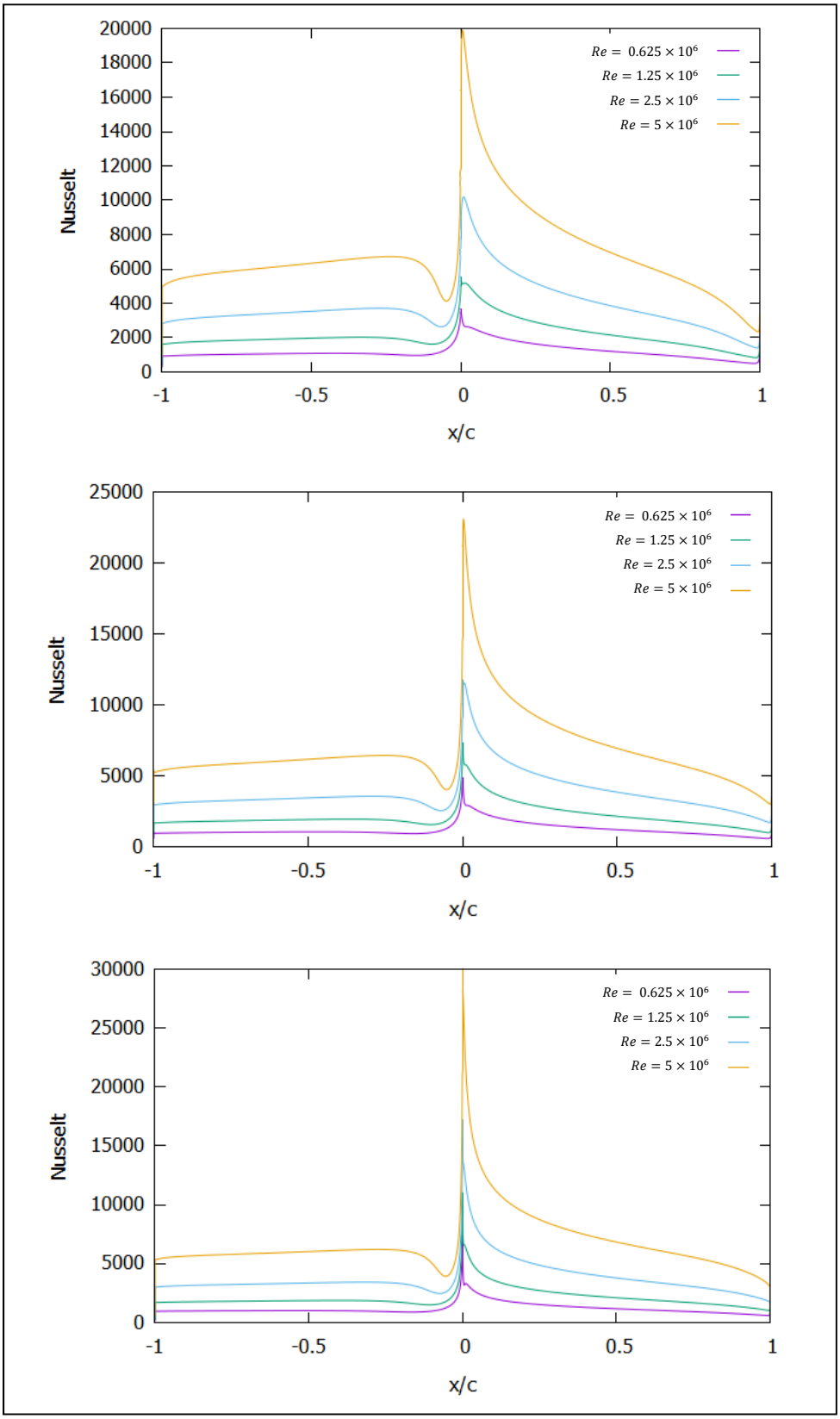

Figure 3.13 Local Nusselt number at the $AOA = 10^{\circ}$ for the NACA 0015, NACA 0012, and NACA 0009 smooth airfoils

3.2 Database

3.2.1 The drag coefficient as a function of the lift coefficient

Results of this section will be used in the next steps to extract the correlation between the lift coefficient and drag coefficient. Figure 3.14 presents the C_d variation as a function of the C_l for the three smooth airfoils at $0^\circ < AOA < 13^\circ$. This study is conducted for Reynolds numbers of $0.625 \times 10^5, 1.2 \times 10^6, 2.5 \times 10^6$ *and* 5×10^6. Based on the figure, the drag coefficient followed an increasing trend based on the lift coefficient increase and based on the increase of the Reynolds number. The maximum drag coefficient is 0.0373 when the lift coefficient is 1.23 with $AOA = 13^\circ$ with a 12% difference to the next highest drag coefficient.

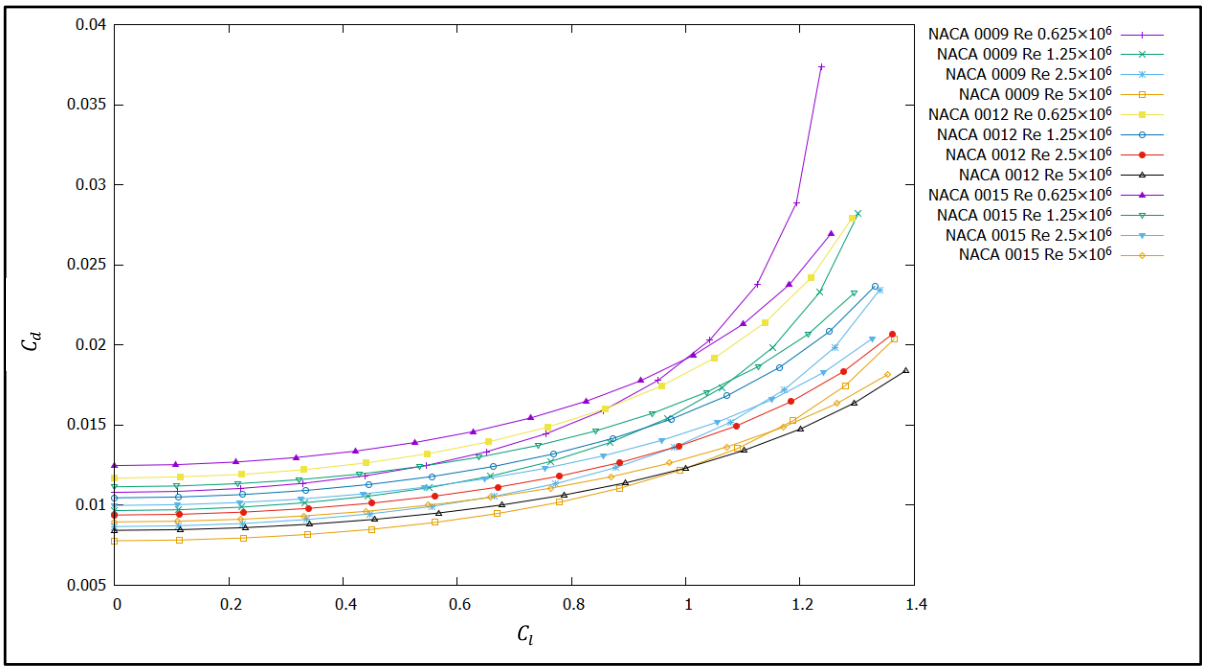

Figure 3.14 Lift coefficient as a function of the drag coefficient for the NACA0009, NACA0012 and NACA0015 smooth airfoils

3.2.2 The average Nusselt number as a function of the lift coefficient

The goal of this thesis is to present a correlation between the average Nusselt number (Nu_{avg}) and the lift coefficient for the smooth and rough surface. Therefore, in this section the results for the Nu_{avg} for the smooth surface NACA0009, NACA0012, and NACA0015 airfoils are studied. Figure 3.15 presents the Nu_{avg} based on the angle of attack. From the figure, the following conclusions are reached. 1- The increase of the average Nusselt number for the smooth surface for all Reynolds numbers. 2- A gradual decrease of the Nu_{avg} with the increase of the angle of attack for all testcases except the NACA0012 and NACA0009 for $0^{\circ} < AOA < 4^{\circ}$.

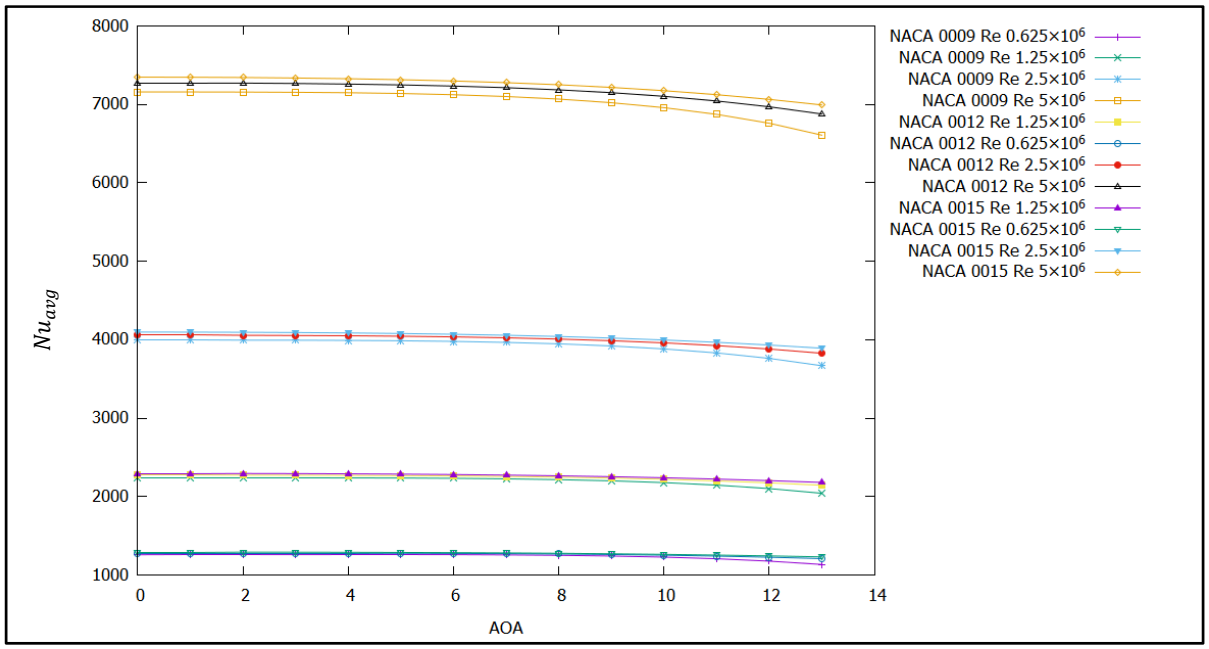

Figure 3.15 Average Nusselt number as a function of the angle of attack for the NACA0009, NACA0012 and NACA0015 smooth airfoils

3.2.3 Aerodynamic correlation

To determine the drag and lift coefficients correlation, the form of Equation (2.40) is used. Figure 3.16 shows the drag coefficient for the three smooth airfoils as a function of the squared lift coefficient. This figure is used to build the correlation in this section. As can be seen at low lift coefficient value, the drag coefficient evolves almost linearly with C_l^2, except for the NACA 0009 at low Reynold's numbers. For high lift coefficients, mostly above 1, the relation between the drag and C_l^2, is not linear anymore.

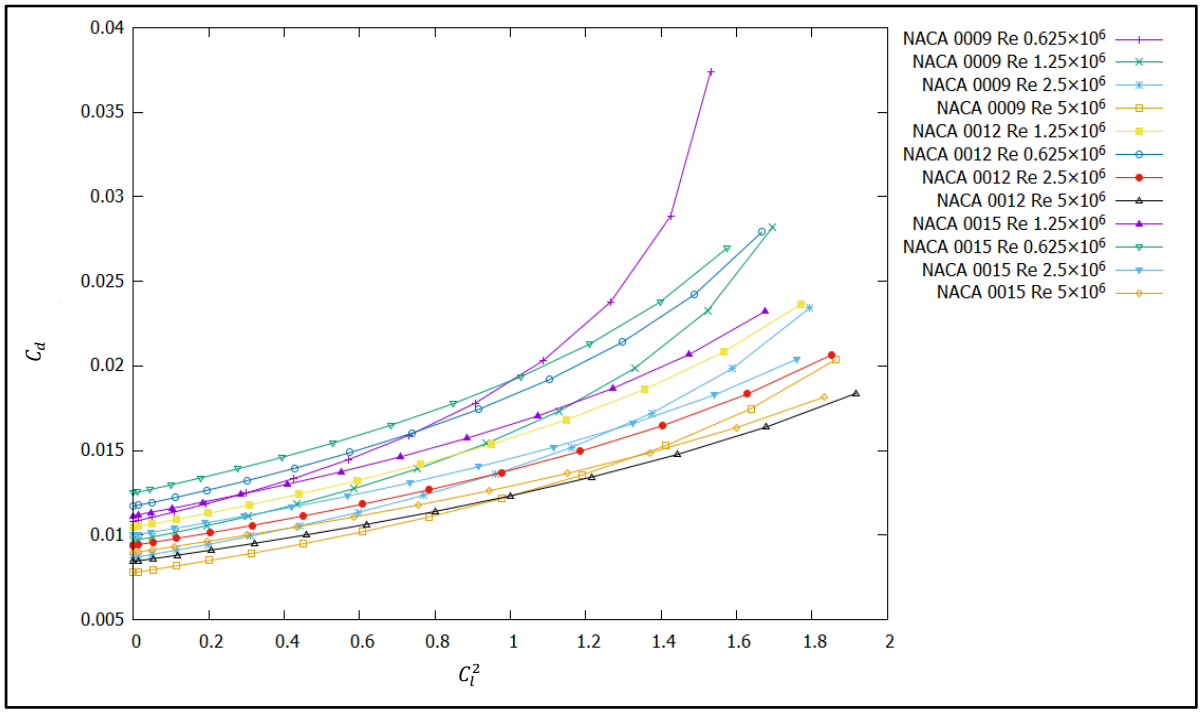

Figure 3.16 Drag coefficient based on the second order lift coefficient for NACA0009, NACA0012 and NACA0015 smooth airfoils

The aerodynamics correlations are derived for different angles of attack, first for the smooth surface and then for the rough surfaces. Figure 3.17 shows the minimum drag coefficient for the smooth surface NACA 0012 and $Re_c \leq 5 \times 10^6$. As shown in Figure 3.17, the minimum drag coefficient decreases with the Reynold's number increase.

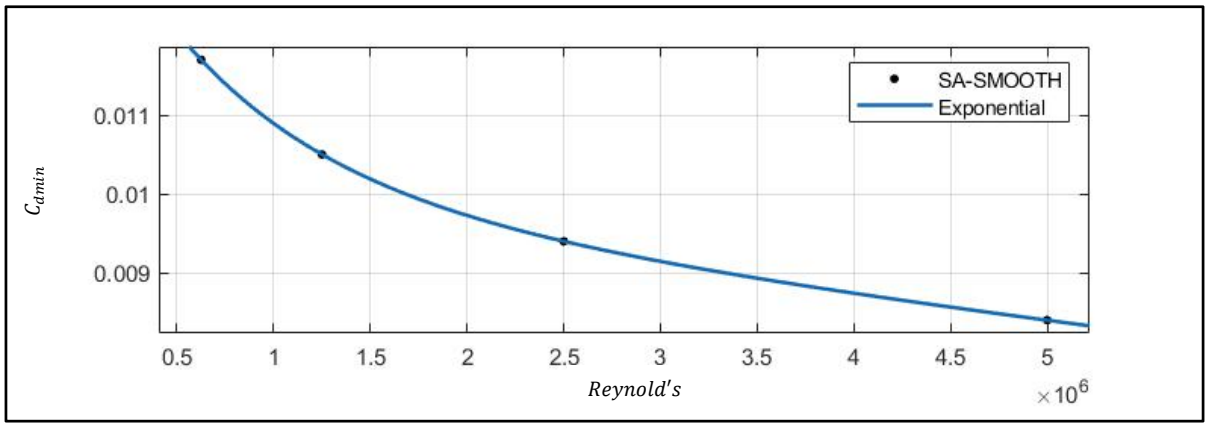

Figure 3.17 Minimum drag coefficient for the NACA 0012 smooth surface $Re \leq 5 \times 10^6$

Based on the curve fitting method (MATLAB, 2019), Equation (3.1) is used to estimate the C_{dmin} at zero angle of attack for $Re_c = 0.625 \times 10^5, 1.2 \times 10^6, 2.5 \times 10^6 \; and \; 5 \times 10^6$. The equation is simplified as an exponential function of Reynolds number to predict the minimum drag coefficient at zero angle of attack for the three airfoils. The coefficients in Equation 3.1 are shown for each airfoil in Table 3-4 and the range of the validity is $Re \leq 5 \times 10^6$.

$$C_{dmin} = a(\exp(b \times Re_c)) + c(\exp(d \times Re_c)) \tag{3.1}$$

Table 3.4 Coefficients in Equation 3.1 for the three smooth airfoils

	NACA 0009	NACA 0012	NACA 0015
a	0.0035	0.004	0.0048
b	-1.23×10^{-6}	-1.29×10^{-6}	-1.51×10^{-6}
c	0.0093	0.01	0.01
d	-3.65×10^{-8}	-3.62×10^{-8}	-3.79×10^{-8}

To add the lift coefficient to the correlation, the Equation (3.2) is used to estimate the C_d for the smooth surface of the NACA0009, NACA0012 and NACA0015 with the fully turbulent condition.

$$C_d = C_{dmin} + (0.00374)\mathrm{C}_l^2 + (0.0012)\mathrm{C}_l^4 \tag{3.2}$$

To include the roughness, Figure 3.18 shows the drag coefficient as a function of the second order lift coefficient for the three rough airfoils. From the results, the overall trend is the increase of the drag coefficient with the lift coefficient increase. For the $Re_c = 2.5 \times 10^6$ and $5 \times 10^6$and for the three airfoils, the results are the same. It means in the rough testcases, results are independent of the Reynolds number after $Re_c = 2.5 \times 10^6$. Although the results of the drag coefficient are independent of the Reynolds number for $Re > 2.5 \times 10^6$, roughness Reynolds number increases with the increase of Reynolds number which is showed in Figure 3.19 for the NACA0012 airfoil with $h_s = 0.00294\, m$ calculated with the maximum sheer velocity on the airfoil using Equation (2.22). From the comparison between Figure 3.16 and 3.18, the overall drag increases with increasing the Reynolds number for the rough surface.

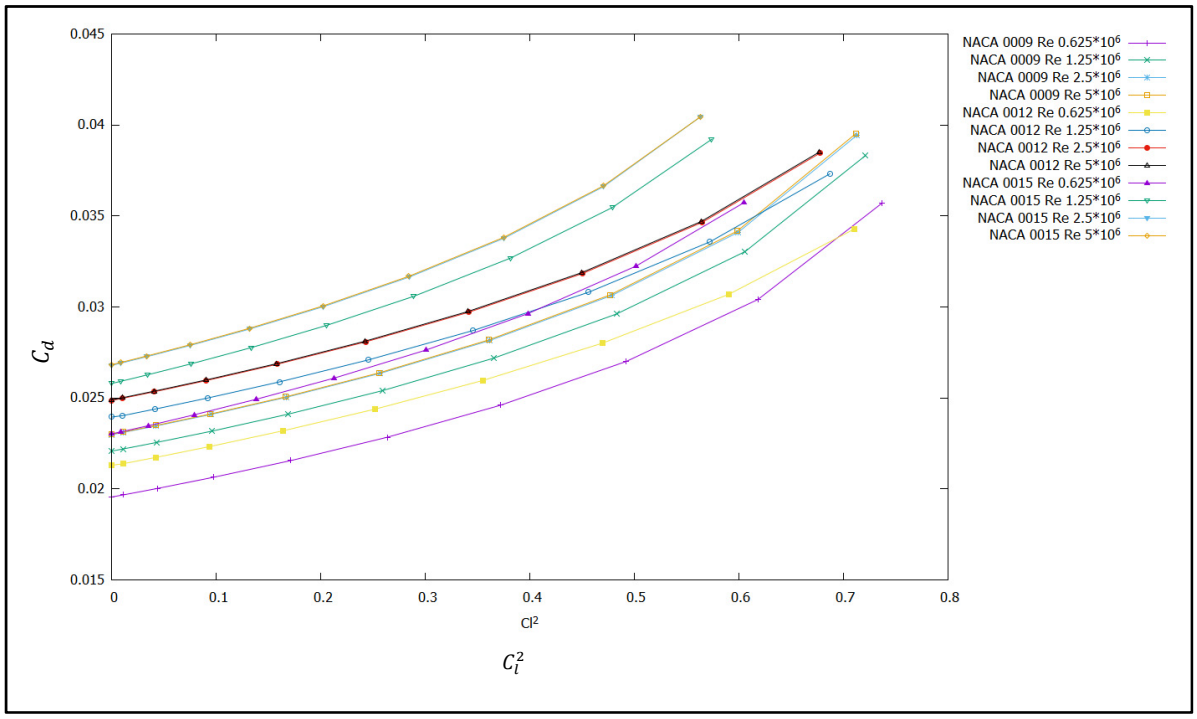

Figure 3.18 Drag coefficient based on the second order lift coefficient for NACA0009, NACA0012 and NACA0015 rough airfoils

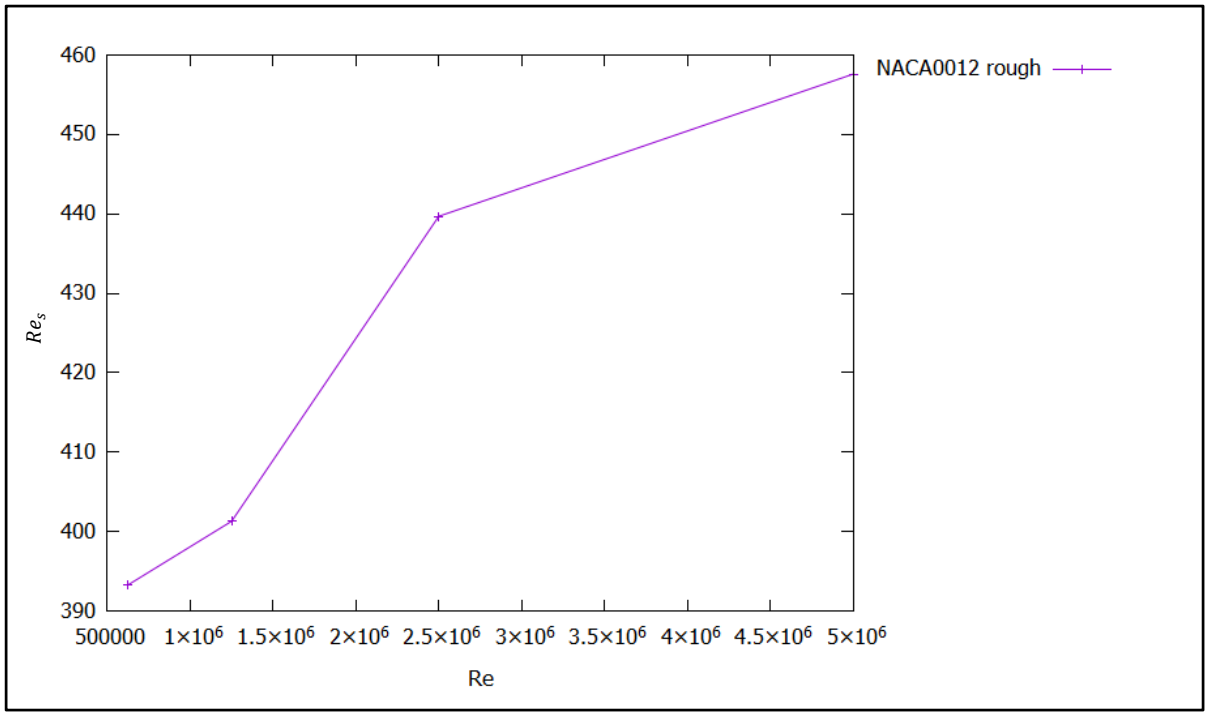

Figure 3.19 Roughness Reynolds number based on Reynolds number for the NACA0012 rough airfoil

Based on the results of the Figure 3.18, to account for the roughness, two separate correlations are needed, one for $Re_c \leq 2.5 \times 10^6$ and one for $Re_c > 2.5 \times 10^6$, which results are independent of the Reynolds number. Figure 3.20 shows the result of the curve fitting using MATLAB with the second order polynomial function of Reynold's number.

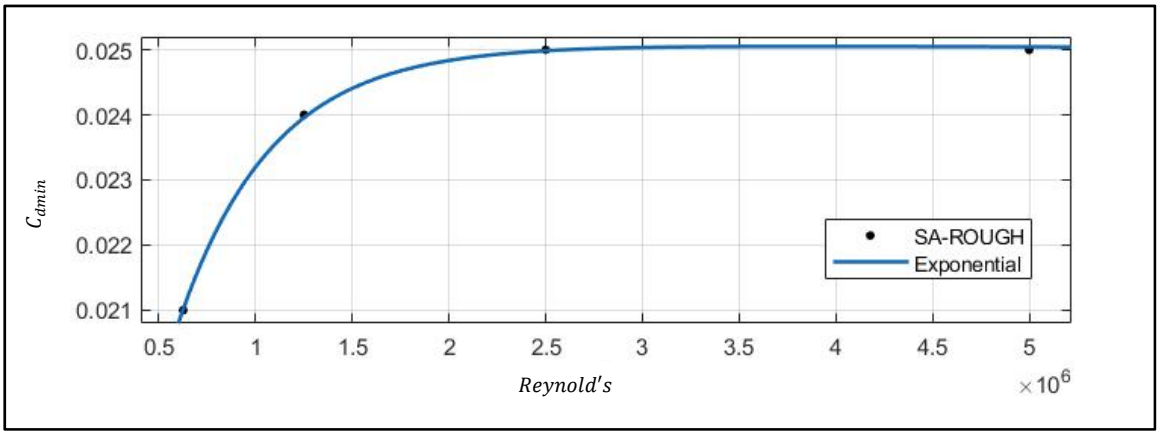

Figure 3.20 Minimum drag coefficient for the NACA 0012 rough surface

Using the curve fitting method, Equation (3.3) is suggested to estimate the C_{dmin} at the zero angle of attack for $Re_c = 0.625 \times 10^5, 1.2 \times 10^6, 2.5 \times 10^6 \; and \; 5 \times 10^6$ with the coefficients shown in Table 3-5

$$C_{dminR} = a(\exp(b \times Re_c) + b(\exp(c \times Re_c) \tag{3.3}$$

Table 3.5 Coefficients in Equation 3.3 for the three rough airfoils

	NACA 0009	NACA 0012	NACA 0015
a	0.023	0.025	0.027
b	-1.81×10^{-10}	-4.08×10^{-10}	-6.54×10^{-10}
c	-0.012	-0.014	-0.013
d	-1.98×10^{-6}	-2.058×10^{-6}	-1.97×10^{-6}

The correlation above would estimate the C_{dminR} which accounts for the roughness with the Equation 3.2 to correlate the lift coefficient to the drag coefficient for the fully rough surface with $h_s = 0.00294\ m$

3.2.4 Heat transfer correlation

In this section, results for the smooth and rough Nusselt number are firstly presented based on the second order lift coefficient. Then, the correlation is derived for the smooth and rough surface similarly to the lift and drag correlations. Figure 3.21 shows the average Nusselt number based on the squared lift coefficient for the three airfoils for $0.625 \times 10^5 < Re_c < 5 \times 10^6$. As can be observed, the results vary almost linearly with the squared lift coefficient, except close to the maximum lift coefficients.

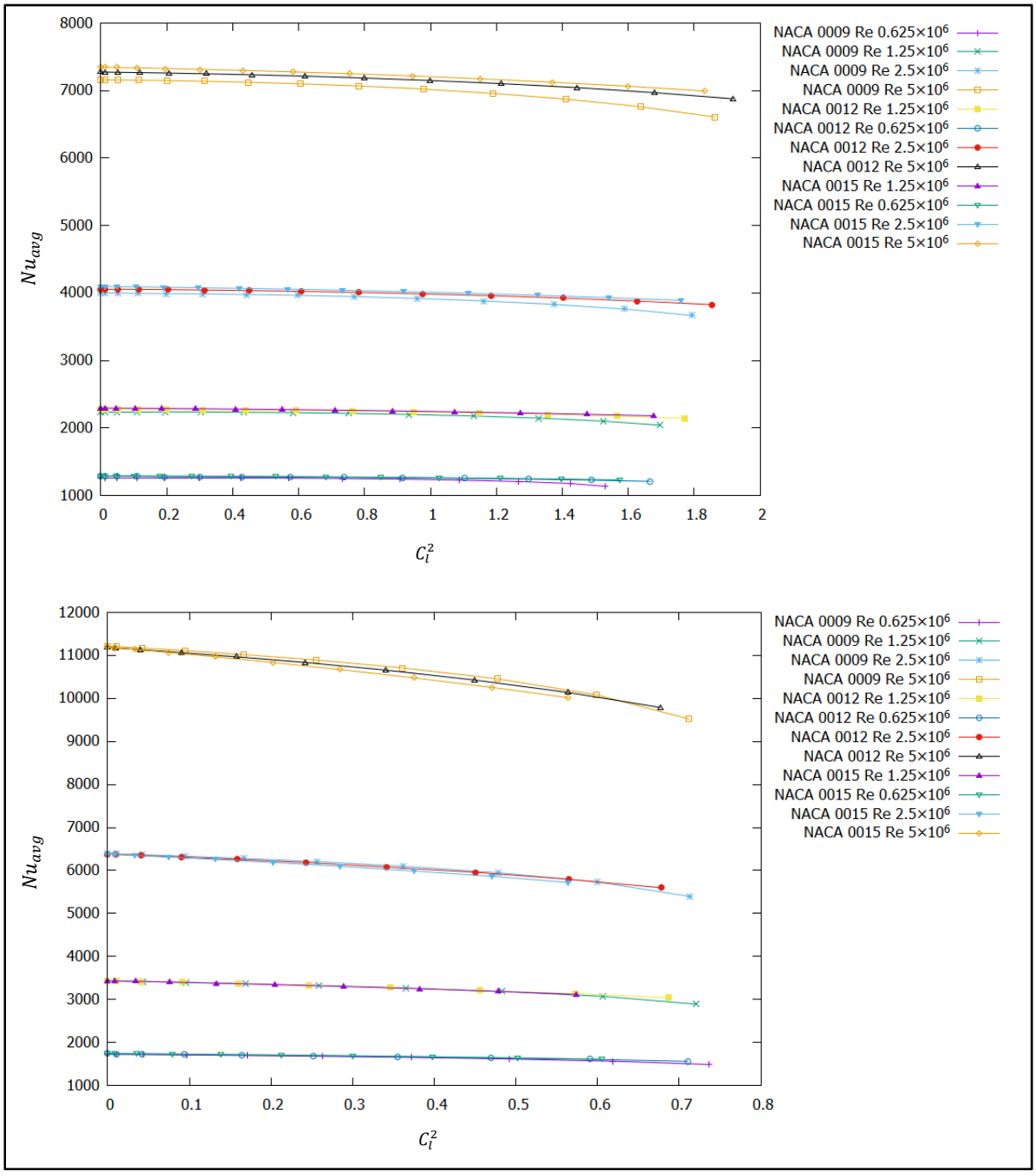

Figure 3.21 NACA 0009, NACA 0012 and NACA 0015 Nu_{avg} variation based on the second order of the lift coefficient for the smooth and rough surface and $0.625 \times 10^5 < Re_c < 5 \times 10^6$.

In order to suggest a correlation for the average Nusselt number, a method similar to the one used by (Wang et al., 2008) is used for the maximum average Nusselt number given by Equation (3.4) for the smooth and (3.5) for the rough surface. The maximum average Nusselt number for the zero angle of attack is predicted based on the curve fitting tool method (MATLAB, 2019). The correlation is valid for the fully turbulent flow with an imposed constant temperature at the wall. As the heat transfer coefficient has a weak dependence on the airfoil thickness, the Nusselt correlations are proposed independent of the airfoil thicknesses.

$$\overline{Nu}_{max} = 0.0195\, Re_c^{0.839} Pr^{\frac{1}{3}} \tag{3.4}$$

$$\overline{Nu}_{maxR} = 0.0233\, Re_c^{0.853} Pr^{\frac{1}{3}} \tag{3.5}$$

With a similar method, Equation 3.6 is suggested to include the lift coefficient into the correlation. Due to the roughness effect on Nusselt number variations for the different Reynolds numbers for rough airfoils, the coefficients for the lift coefficient are dependant on the Reynolds number. The equation is valid for the fully turbulent flow between $0.625 \times 10^5 < Re_c < 5 \times 10^6$ and $0^\circ < AOA < 13^\circ$ for the smooth and $0^\circ < AOA < 9^\circ$ for the rough surface. Figure 3.22 shows the results of the average Nusselt number correlation for the smooth and rough NACA 0012 and $Re_c = 1.25 \times 10^6$. As the results show, the maximum discrepancy between the predicted correlation and CFD results for the smooth and rough surfaces occurs at the highest angle of attack and the value is less than 1%.

$$\overline{Nu} = \overline{Nu}_{max} - (0.00021 \times Re_c)\, C_L^2 - (0.00033 \times Re_c)\, C_L^4 \tag{3.6}$$

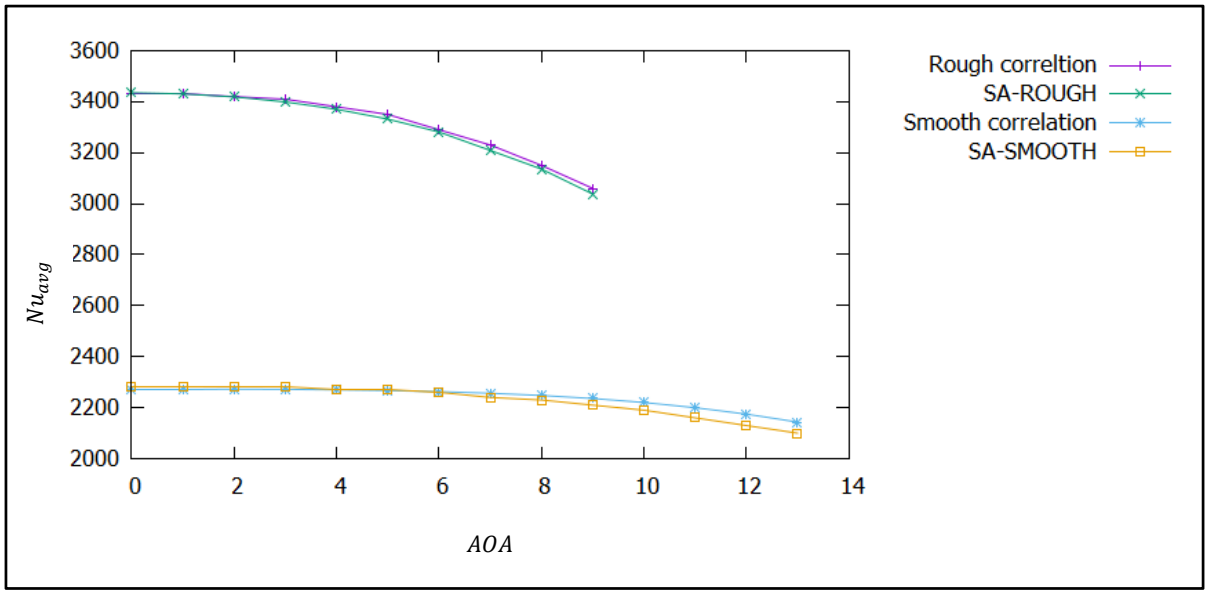

Figure 3.22 Curve fitting attempt for the rough and smooth surfaces for the NACA 0009, NACA 0012, and NACA 0015 for $Re_c = 1.25 \times 10^6$

3.3 Analysis

Results of the average Nusselt correlations are discussed in this section with the numerical work of (Samad, 2021). In his work, he suggested a correlation between the average Frossling number as a function of the angle of attack and the Reynolds number for the smooth NACA 0012 airfoil. Based on the CFD results, the correlation for the $1 \times 10^5 \leq Re_c \leq 3 \times 10^6$ and $0^{\circ} \leq AOA \leq 30^{\circ}$ is as follows:

$$\overline{Fr} = 0.021(1 + 1.131\alpha - 8.634\alpha^2 + 10\alpha^3)Re_c{}^{0.335}Pr^{1/3} \tag{3.7}$$

For the analysis of the heat transfer results, the Samad's correlation is plotted and compared to the correlation based on the lift coefficient presented in Equation 3.7 and with the $\overline{Nu}_{max}$ for

the smooth surface of Equation 3.6. Results for heat transfer correlations are for $Re_c = 1 \times 10^6$ and are presented in Figure 3.23.

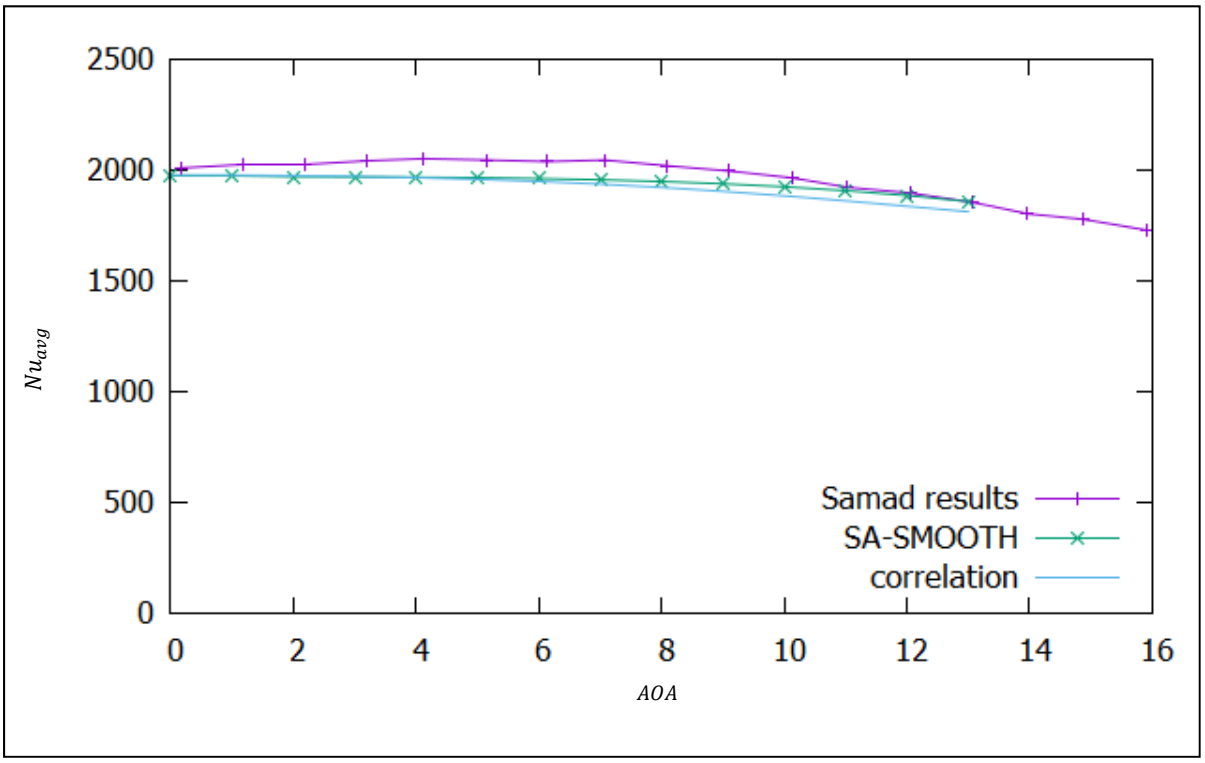

Figure 3.23 Verification of the Nusselt number prediction based on the correlation

The average discrepancy between the SA-SMOOTH CFD and Samad's results is 3.3%. The predicted correlation indicated in Equation 3.6 has a better agreement at the low angles of attack rather than high angles for the NACA 0012 airfoil. For the correlation and SA-SMOOTH results, a gradual decrease in seen while for the Samad's Nusselt correlation, the trend is an increase up to the $AOA = 5^\circ$ followed by a decreasing trend for the highest angle of attack test case.

3.4 Summary

For the NACA0009 airfoil, the smooth CFD results were compared to the Xfoil prediction (Drela, 1989). The NACA0012 airfoil results for the smooth surface were compared to the OVERFLOW CFD results (Jespersen et al., 2016) and validated with Ladson experiments. The rough NACA0012 results were compared to the work of (Tagawa, 2021). The NACA0015 airfoil results are compared and validated with the results of (Joslin et al., 1999) and (Gilling & Sørensen, 2008). The heat transfer validation were conducted with the NACA0012 airfoil against the work of (Samad, 2021) and (Poinsatte et al., 1990). The comparisons showed a good concordance estimation with the CFD.

Following the validation, the effect of the Reynolds number on the heat transfer coefficient is studied and the database is built for the lift coefficient, drag coefficient and the average Nusselt number. Based on these results, two correlations are proposed. First the correlation between the lift and drag coefficients for the smooth and rough surfaces. Then, the correlation between the average Nusselt number and the lift coefficient for the smooth and rough surfaces. The correlations are valid for the fully turbulent flow, $0.625 \times 10^5 < Re_c < 5 \times 10^6$ and $0^\circ < AOA < 13^\circ$ for the smooth and $0^\circ < AOA < 9^\circ$ for the rough surface. Finally, a correlation for the average Nusselt number correlation is successfully compared with the work of (Samad, 2021) for the smooth NACA 0012 airfoil.

The results of the CFD calculation are compared and validated before being used to build the database and the two correlations based on the aerodynamic and heat transfer coefficients. The three mesh density properties were presented. The GCI method was used to select a high-quality mesh to be used to build the database and to estimate the numerical error. Then, the angle of attack for the maximum lift coefficient is calculated.

CONCLUSION

As today, the safety of aircrafts has increased significantly but aircraft icing is still one of the most important aviation problems. The reason of this importance is not only the degradation of aircraft aerodynamic performances but it is also the malfunctioning of the pneumatic and hydraulic control surfaces of aircrafts because of the ice accretion. Therefore, many scientists have tried to study the problem of icing, either by modelling ice or by conducting test flights under icing conditions.

In this thesis, the CFD method is used to predict the aerodynamics and heat transfer of airfoils. CFD as a high-fidelity method solves the Navier-Stokes equations numerically. The proposed model uses the RANS Spalart-Allmaras equations for the smooth and the modified Spalart-Allmaras equations that considers the roughness of the iced airfoils. The CFD results named SA-SMOOTH and SA-ROUGH were validated with numerical and experimental results available in the literature. CFD calculations were conducted with four different Reynolds number, using three airfoils (NACA 0009, 0012 and 0015) with smooth and rough surfaces and over different angles of attack.

Using the above CFD results, a database containing aerodynamic and heat transfer results has been created, allowing to propose two correlations for the drag and lift coefficients. The proposed equation is valid for the fully turbulent flow for $0.625 \times 10^5 < Re_c < 5 \times 10^6$ and $0^\circ < AOA < 13^\circ$ for the smooth and $0^\circ < AOA < 9^\circ$ for the rough surfaces. Moreover, two Nusselt number correlations have been proposed (one for smooth surface and one for rough surface). The proposed heat transfer correlations were successfully compared to results from the literature with an average discrepancy of 3.3%.

In future work, it is suggested to study the influence of the turbulence model on the proposed correlations. It is also suggested to pursue 3D de-icing CFD modeling using different ice shapes to derive heat transfer correlations over iced rough surfaces.

APPENDIX I

Configuration used for Xfoil

The following configuration is set to extract the data from the Xfoil prediction:

$Reynolds$: 1000000

$Ncrit = 5$

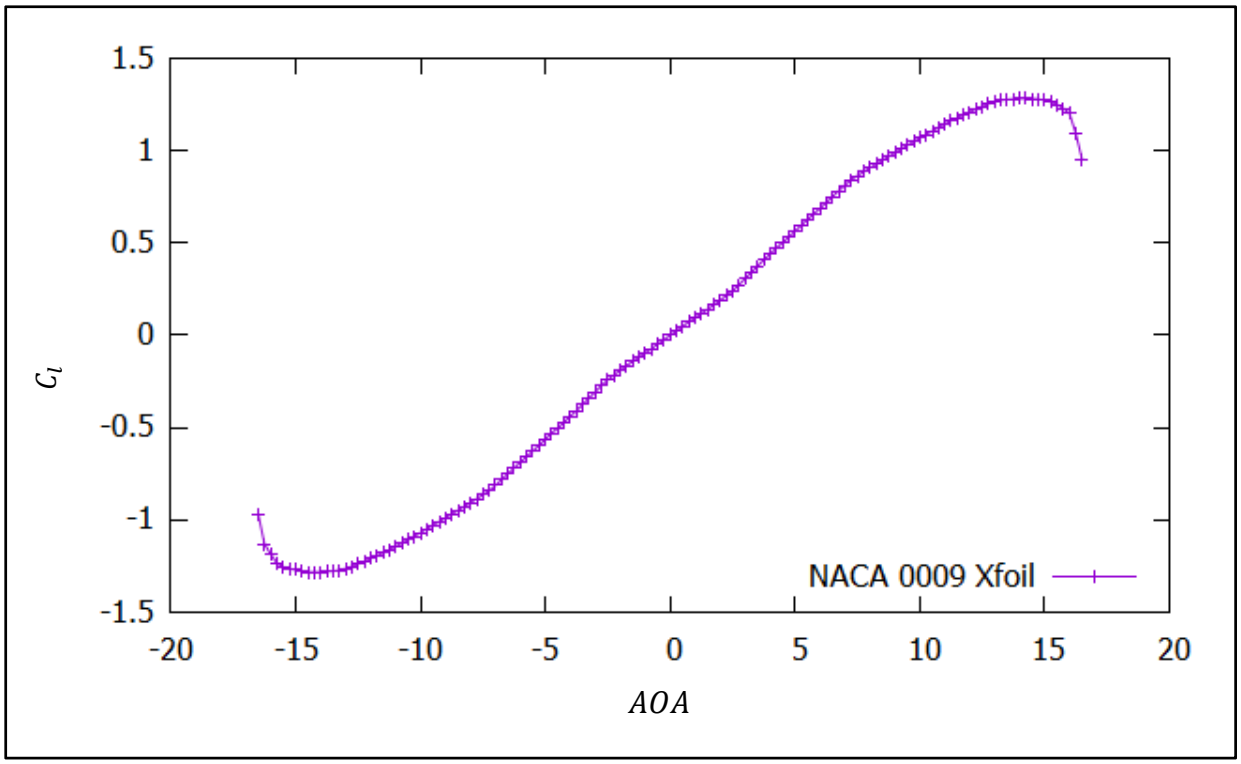

Figure-A I.1 Xfoil prediction for the NACA 0009

BIBLIOGRAPHY

Anderson, D., & Shin, J. (1997). Characterization of ice roughness from simulated icing encounters. In *35th Aerospace Sciences Meeting and Exhibit* (pp. 52). DOI: 10.2514/6.1997-52. Retrieved from https://ntrs.nasa.gov/api/citations/19970009633/downloads/19970009633.pdf

Anderson, J. (2011). *EBOOK: Fundamentals of Aerodynamics (SI units)*. McGraw Hill.

Anderson, J. D. (1999). *Aircraft performance and design* (Vol. 1). WCB/McGraw-Hill Boston. Retrieved from https://books.google.ca/books/about/Aircraft_Performance_Design.html?id=PwtO7aiwbBwC&redir_esc=y

Aupoix, B. (2015). Improved heat transfer predictions on rough surfaces. *International Journal of Heat and Fluid Flow, 56*, 160-171. Retrieved from https://doi.org/10.1016/j.ijheatfluidflow.2015.07.007

Aupoix, B., & Spalart, P. (2003). Extensions of the Spalart–Allmaras turbulence model to account for wall roughness. *International Journal of Heat and Fluid Flow, 24*(4), 454-462. DOI: https://doi.org/10.1016/S0142-727X(03)00043-2

Battisti, L., Zanne, L., Castelli, M. R., Bianchini, A., & Brighenti, A. (2020). A generalized method to extend airfoil polars over the full range of angles of attack. *Renewable Energy, 155*, 862-875. DOI: https://doi.org/10.1016/j.renene.2020.03.150

Beaugendre, H., Morency, F., Habashi, W. G., & Benquet, P. (2003). Roughness implementation in FENSAP-ICE: Model calibration and influence on ice shapes. *Journal of aircraft, 40*(6), 1212-1215. DOI: https://doi.org/10.2514/2.7214

Beisbart, C., & Saam, N. J. (2019). *Computer simulation validation*. Springer. DOI: https://doi.org/10.1007/978-3-319-70766-2

Bergman, T. L., Incropera, F. P., DeWitt, D. P., & Lavine, A. S. (2011). *Fundamentals of heat and mass transfer*. John Wiley & Sons. Retrieved from https://books.google.ca/books/about/Fundamentals_of_Heat_and_Mass_Transfer.html?id=vvyIoXEywMoC#:~:text=Fundamentals%20of%20Heat%20and%20Mass%20Transfer%2C%207th%20Edition%20is%20the,transfer%20education%2C%20research%20and%20practice.

Bianchini, A., Balduzzi, F., Rainbird, J. M., Peiro, J., Graham, J. M. R., Ferrara, G., & Ferrari, L. (2016). An experimental and numerical assessment of airfoil polars for use in Darrieus wind turbines—Part II: Post-stall data extrapolation methods. *Journal of*

Engineering for Gas Turbines and Power, 138(3). DOI: https://doi.org/10.1115/1.4031270

Blazek, J. (2015). *Computational fluid dynamics: principles and applications*. Butterworth-Heinemann. Retrieved from https://www.sciencedirect.com/book/9780080999951/computational-fluid-dynamics-principles-and-applications

Bove, S. (2008). *Lswt report of campaign naca 0015_1*. Technical report, LM Glasfiber, Lunderskov.

Bragg, M. B. (1981). *Rime ice accretion and its effect on airfoil performance* (The Ohio State University). Rtrieved from https://ntrs.nasa.gov/citations/19820016290

Bragg, M. B., Broeren, A. P., & Blumenthal, L. A. (2005). Iced-airfoil aerodynamics. *Progress in Aerospace Sciences, 41*(5), 323-362. DOI: https://doi.org/10.1016/j.paerosci.2005.07.001

Broeren, A. P., Potapczuk, M., Riley, J., Villedieu, P., Moëns, F., & Bragg, M. (2013). Swept-wing ice accretion characterization and aerodynamics. In *5th AIAA Atmospheric and Space Environments Conference* (pp. 2824). Retrieved from https://ntrs.nasa.gov/api/citations/20140009586/downloads/20140009586.pdf

Buck, C. R. (2008). Safety advisor. *Weather no. l. AOPA online documents*. Retrieved from http://www.aopa.org/asf/nubli-eations/sall

Cao, Y., Wu, Z., Su, Y., & Xu, Z. (2015). Aircraft flight characteristics in icing conditions. *Progress in Aerospace Sciences, 74*, 62-80. DOI: https://doi.org/10.1016/j.paerosci.2014.12.001

Carroll, T., & McAvoy, W. H. (1929). *The Formation of Ice Upon Airplanes in Flight*. Retrieved from https://ntrs.nasa.gov/citations/19930081134

Davidson, L. (2018). Fluid mechanics, turbulent flow and turbulence modeling. *Chalmers University of Technology, Goteborg, Sweden (Nov 2011)*. Retrieved from http://www.tfd.chalmers.se/~lada/postscript_files/solids-and-fluids_turbulent-flow_turbulence-modelling.pdf

Dipprey, D. F., & Sabersky, R. H. (1963). Heat and momentum transfer in smooth and rough tubes at various Prandtl numbers. *International Journal of Heat and Mass Transfer, 6*(5), 329-353. DOI: https://doi.org/10.1016/0017-9310(63)90097-8

Drela, M. (1989). XFOIL: An analysis and design system for low Reynolds number airfoils. In *Low Reynolds number aerodynamics* (pp. 1-12). Springer. DOI: https://doi.org/10.1007/978-3-642-84010-4_1

FAA. (2019). *Helicopter Flying Handbook*. Retrieved from https://www.faa.gov/regulations_policies/handbooks_manuals/aviation/helicopter_flying_handbook/media/hfh_front.pdf

Gilling, L., & Sørensen, N. (2008). Large eddy simulations of an airfoil in turbulent inflow. In *4th PhD Seminar on Wind Energy in Europe: Book of Abstracts* (pp. 33-36). The European Wind Energy Association. Retrieved from https://www.researchgate.net/publication/236888745_Detached_Eddy_Simulations_of_an_Airfoil_in_Turbulent_Inflow

Götten, F., Havermann, M., Braun, C., Marino, M., & Bil, C. (2020). Airfoil drag at low-to-medium reynolds numbers: A novel estimation method. *AIAA journal, 58*(7), 2791-2805. DOI: https://doi.org/10.2514/1.J058983

Gray, V. H. (1958). *Correlations among ice measurements, impingement rates icing conditions, and drag coefficients for unswept NACA 65A004 airfoil*. Retrieved from https://ntrs.nasa.gov/citations/19810068588

Green, S. (2006). A study of US inflight icing accidents and incidents, 1978 to 2002. In *44th AIAA Aerospace Sciences Meeting and Exhibit* (pp. 82). DOI: https://doi.org/10.2514/6.2006-82

Gudmundsson, S. (2013). *General aviation aircraft design: Applied Methods and Procedures*. Butterworth-Heinemann. Retrieved from https://www.sciencedirect.com/book/9780123973085/general-aviation-aircraft-design

Guffond, D., & Brunet, L. (1988). Validation du programme bidimensionnel de capitation. *ONERA RP, 20*, 5146.

Gulick, B. G. (1938). *Effects of a Simulated Ice Formation on the Aerodynamic Characteristics of an Airfoil*. Retrieved from https://ntrs.nasa.gov/citations/19930093051

Han, Y., & Palacios, J. (2017). Surface roughness and heat transfer improved predictions for aircraft ice-accretion modeling. *AIAA journal, 55*(4), 1318-1331. DOI: https://doi.org/10.2514/1.J055217

Healzer, J., Moffat, R., & Kays, W. (1974). The turbulent boundary layer on a porous, rough plate-experimentalheat transfer with uniform blowing. In *Thermophysics and Heat Transfer Conference* (pp. 680). Retrieved from https://apps.dtic.mil/sti/citations/ADA020530

Henry, R. C., Guffond, D., Garnier, F., & Bouveret, A. (2000). Heat transfer coefficient measurement on iced airfoil in small icing wind tunnel. *Journal of thermophysics and heat transfer, 14*(3), 348-354. Retrieved from https://arc.aiaa.org/doi/10.2514/2.6551

Hilpert, R. (1933). Heat transfer from cylinders. *Forsch. Geb. Ingenieurwes, 4*(5), 215.

Hoerner, S. F. (1965). Fluid Dynamic Drag, published by the author. *Midland Park, NJ*, 16-35. Retrieved from http://ftp.demec.ufpr.br/disciplinas/TM240/Marchi/Bibliografia/Hoerner.pdf

Jespersen, D. C., Pulliam, T. H., & Childs, M. L. (2016). *Overflow turbulence modeling resource validation results*. DOI: https://ntrs.nasa.gov/citations/20190000252

Joslin, R., Horta, L., & Chen, F. (1999). Transiting action control to application. In *Proceedings of the 30th AIAA Fluid Dynamics Conference, Norfolk, VA, USA* (Vol. 28). Retrieved from https://citeseerx.ist.psu.edu/viewdoc/download?doi=10.1.1.45.4228&rep=rep1&type=pdf

Kays, W. M. (2012). *Convective heat and mass transfer*. Tata McGraw-Hill Education.

Kitamura, K., & Shima, E. (2013). Towards shock-stable and accurate hypersonic heating computations: A new pressure flux for AUSM-family schemes. *Journal of Computational Physics, 245*, 62-83. DOI: https://doi.org/10.1016/j.jcp.2013.02.046

Kundu, P. K., Cohen, I. M., & Dowling, D. R. (2015). *Fluid mechanics*. Academic press. Retrieved from https://www.elsevier.com/books/fluid-mechanics/kundu/978-0-12-405935-1

Ladson, C. L. (1988). *Effects of independent variation of Mach and Reynolds numbers on the low-speed aerodynamic characteristics of the NACA 0012 airfoil section* (Vol. 4074). National Aeronautics and Space Administration, Scientific and Technical …. Retrieved from https://ntrs.nasa.gov/citations/19880019495

Launder, B. E., & Spalding, D. B. (1983). The numerical computation of turbulent flows. In *Numerical prediction of flow, heat transfer, turbulence and combustion* (pp. 96-116). Elsevier. DOI: https://doi.org/10.1016/0045-7825(74)90029-2

Link, N. K., Kruk, R. V., McKay, D., Jennings, S. A., & Craig, G. (2002). Hybrid enhanced and synthetic vision system architecture for rotorcraft operations. In *Enhanced and Synthetic Vision 2002* (Vol. 4713, pp. 190-201). SPIE.

Liu, Y., & Hu, H. (2018). An experimental investigation on the unsteady heat transfer process over an ice accreting airfoil surface. *International Journal of Heat and Mass Transfer, 122*, 707-718.

Lynch, F. T., & Khodadoust, A. (2001). Effects of ice accretions on aircraft aerodynamics. *Progress in Aerospace Sciences, 37*(8), 669-767. DOI: https://doi.org/10.1016/S0376-0421(01)00018-5

MATLAB. (2019). Solve nonlinear least-squares (nonlinear data-fitting) problems. Retrieved from https://www.mathworks.com/help/optim/ug/lsqnonlin.html

Molina, E., Spode, C., Annes da Silva, R. G., Manosalvas-Kjono, D. E., Nimmagadda, S., Economon, T. D., . . . Righi, M. (2017). Hybrid rans/les calculations in su2. In *23rd AIAA computational fluid dynamics conference* (pp. 4284). DOI: https://doi.org/10.2514/6.2017-4284

Montreuil, E., Chazottes, A., Guffond, D., Murrone, A., Caminade, F., & Catris, S. (2009). 1 Enhancement of Prediction Capability in Icing Accretion and related Performance Penalties Part I: Three-dimensional CFD Prediction of the Ice Accretion.

Morency, F., & Beaugendre, H. (2020). Comparison of turbulent Prandtl number correction models for the Stanton evaluation over rough surfaces. *International Journal of Computational Fluid Dynamics, 34*(4), 278-298. DOI: https://doi.org/10.1080/10618562.2020.1753712

Nikuradse, J. (1950). Laws of flow in rough pipes. Retrieved from https://ntrs.nasa.gov/citations/19930093938

NTSB. (1994). *Aircraft accident report*. Roselawn, Indiana: National Transportation Safety Board. Retrieved from https://www.ntsb.gov/investigations/AccidentReports/Reports/AAR9601.pdf

Palacios, F., Colonno, M. R., Aranake, A. C., Campos, A., Copeland, S. R., Economon, T. D., . . . Alonso, J. J. (2013). Stanford University Unstructured (SU2): An open-source integrated computational environment for multi-physics simulation and design. *AIAA paper, 287*, 2013. DOI: https://doi.org/10.2514/6.2013-287

Poinsatte, P. E., Van Fossen, G. J., & De Witt, K. J. (1990). Convective heat transfer measurements from a NACA 0012 airfoil in flight and in the NASA Lewis Icing Research Tunnel. In *28th Aerospace Sciences Meeting* (pp. 199). Retrieved from https://ntrs.nasa.gov/api/citations/19900004434/downloads/19900004434.pdf

Poinsatte, P. E., Van Fossen, G. J., & De Witt, K. J. (1991). Roughness effects on heat transfer from a NACA 0012 airfoil. *Journal of aircraft, 28*(12), 908-911. DOI: https://doi.org/10.2514/3.46116

Ratvasky, T. P., Barnhart, B. P., & Lee, S. (2010). Current methods modeling and simulating icing effects on aircraft performance, stability, control. *Journal of aircraft, 47*(1), 201-

211. Retrieved from https://ntrs.nasa.gov/api/citations/20110016128/downloads/20110016128.pdf

Roache, P. J. (1994). Perspective: a method for uniform reporting of grid refinement studies. DOI: https://doi.org/10.1115/1.2910291

Samad, A. (2021). *Modeling effects of external convective heat transfer on rotating blades in anti-icing operations* (École de technologie supérieure). Rtrieved from https://espace.etsmtl.ca/id/eprint/2744/

Spalart, P., & Allmaras, S. (1992). A one-equation turbulence model for aerodynamic flows. In *30th aerospace sciences meeting and exhibit* (pp. 439). DOI: https://doi.org/10.2514/6.1992-439

Suga, K., Craft, T., & Iacovides, H. (2006). An analytical wall-function for turbulent flows and heat transfer over rough walls. *International Journal of Heat and Fluid Flow, 27*(5), 852-866. DOI: https://doi.org/10.1016/j.ijheatfluidflow.2006.03.011

Tagawa, G. B., Morency, F., & Beaugendre, H. (2021). CFD investigation on the maximum lift coefficient degradation of rough airfoils. *AIMS Energy, 9*(2), 305-325.

Tagawa, G. B. S. (2021). CFD investigation on the maximum lift coefficient degradation of rough airfoils. *AIMS Energy, 9*(2), 305. DOI: https://doi.org/10.3934/energy.2021016

Thomas, S. K., Cassoni, R. P., & MacArthur, C. D. (1996). Aircraft anti-icing and de-icing techniques and modeling. *Journal of aircraft, 33*(5), 841-854. DOI: https://doi.org/10.2514/3.47027

Tinoco, E., Bogue, D., Kao, T., Yu, N., Li, P., & Ball, D. (2005). Progress toward CFD for full flight envelope. *The Aeronautical Journal, 109*(1100), 451-460. Retrieved from https://www.cambridge.org/core/journals/aeronautical-journal/article/progress-toward-cfd-for-full-flight-envelope/8D0D3EA36A307E597E26FA2CBA73758A

Transport-Canada. (2019). *Guidelines for Aircraft Ground Icing Operations*. Retrieved from https://tc.canada.ca/sites/default/files/migrated/tp14052e___4th_edition__summer_2019.pdf

Villeneuve, E., Samad, A., Volat, C., Béland, M., & Lapalme, M. (2022). An Experimental Apparatus for Icing Tests of Low Altitude Hovering Drones. *Drones, 6*(3), 68. DOI: https://doi.org/10.3390/drones6030068

Wang, X., Naterer, G., & Bibeau, E. (2008). Convective heat transfer from a NACA airfoil at varying angles of attack. *Journal of thermophysics and heat transfer, 22*(3), 457-463. DOI: https://doi.org/10.2514/1.34405

Wright, W. (2008). User Manual for LEWICE Ver. 3.2. *NASA CR, 214255*. Retrieved from https://ntrs.nasa.gov/search.jsp?R=20080048307

Zhang, X., & Romzek, M. (2008). *Computational fluid dynamics (CFD) applications in vehicle exhaust system*. SAE Technical Paper.

Zhang, Y., Habashi, W. G., & Khurram, R. A. (2016). Zonal detached-eddy simulation of turbulent unsteady flow over iced airfoils. *Journal of aircraft, 53*(1), 168-181. DOI: https://doi.org/10.2514/1.C033253